SIAM J. SCI. COMPUT.
Vol. 35, No. 6, pp. A2671–A2695

A SIMPLE AND EFFICIENT NUMERICAL METHOD FOR COMPUTING THE DYNAMICS OF ROTATING BOSE–EINSTEIN CONDENSATES VIA ROTATING LAGRANGIAN COORDINATES*

WEIZHU BAO†, DANIEL MARAHRENS‡, QINGLIN TANG†, AND YANZHI ZHANG§

Abstract. We propose a simple, efficient, and accurate numerical method for simulating the dynamics of rotating Bose–Einstein condensates (BECs) in a rotational frame with or without long-range dipole-dipole interaction (DDI). We begin with the three-dimensional (3D) Gross–Pitaevskii equation (GPE) with an angular momentum rotation term and/or long-range DDI, state the two-dimensional (2D) GPE obtained from the 3D GPE via dimension reduction under anisotropic external potential, and review some dynamical laws related to the 2D and 3D GPEs. By introducing a rotating Lagrangian coordinate system, the original GPEs are reformulated to GPEs without the angular momentum rotation, which is replaced by a time-dependent potential in the new coordinate system. We then cast the conserved quantities and dynamical laws in the new rotating Lagrangian coordinates. Based on the new formulation of the GPE for rotating BECs in the rotating Lagrangian coordinates, a time-splitting spectral method is presented for computing the dynamics of rotating BECs. The new numerical method is explicit, simple to implement, unconditionally stable, and very efficient in computation. It is spectral-order accurate in space and second-order accurate in time and conserves the mass on the discrete level. We compare our method with some representative methods in the literature to demonstrate its efficiency and accuracy. In addition, the numerical method is applied to test the dynamical laws of rotating BECs such as the dynamics of condensate width, angular momentum expectation, and center of mass, and to investigate numerically the dynamics and interaction of quantized vortex lattices in rotating BECs without or with the long-range DDI.

Key words. rotating Bose–Einstein condensate, dipole-dipole interaction, Gross–Pitaevskii equation, angular momentum rotation, rotating Lagrangian coordinates, time-splitting

AMS subject classifications. 35Q41, 65M70, 81Q05, 81V45, 82D50

DOI. 10.1137/130911111

1. Introduction.

Bose–Einstein condensation (BEC), first observed in 1995 [4, 18, 23], has provided a platform to study the macroscopic quantum world. Later, with the observation of quantized vortices [2, 19, 34, 35, 37, 39, 50], rotating BECs have been extensively studied in the laboratory. The occurrence of quantized vortices is a hallmark of the superfluid nature of BECs. In addition, condensation of bosonic atoms and molecules with significant dipole moments whose interaction is both nonlocal and anisotropic has recently been achieved experimentally in trapped ^{52}Cr and ^{164}Dy gases [1, 22, 27, 32, 33, 36, 48].

At temperatures T much smaller than the critical temperature T_c, the properties of BEC in a rotating frame with long-range dipole-dipole interaction (DDI) are well

*Submitted to the journal's Methods and Algorithms for Scientific Computing section February 26, 2013; accepted for publication (in revised form) September 17, 2013; published electronically November 19, 2013.

http://www.siam.org/journals/sisc/35-6/91111.html

†Department of Mathematics and Center for Computational Science and Engineering, National University of Singapore, Singapore 119076 (bao@math.nus.edu.sg, http://www.math.nus.edu.sg/~bao; mattq@nus.edu.sg). This research was supported by the Singapore A*STAR SERC "Complex Systems" Research Programme grant 1224504056.

‡Max Planck Institute for Mathematics in the Sciences, Inselstr. 22, 04103 Leipzig, Germany (Daniel.Marahrens@mis.mpg.de). This author's work was supported by research award KUK-I1-007-43 from King Abdullah University of Science and Technology (KAUST).

§Department of Mathematics and Statistics, Missouri University of Science and Technology, Rolla, MO 65409-0020 (zhangyanz@mst.edu). This author's work was supported by the University of Missouri Research Board, Simons Foundation award 210138, and NSF grant DMS-1217000.

described by the macroscopic complex-valued wave function $\psi = \psi(\mathbf{x}, t)$ whose evolution is governed by the three-dimensional (3D) Gross–Pitaevskii equation (GPE) with an angular momentum rotation term and long-range DDI [1, 10, 20, 26, 30, 31, 41, 47, 49, 54]. In dimensionless form, the 3D GPE has the form

$$i\partial_t \psi(\mathbf{x}, t) = \left[-\frac{1}{2}\nabla^2 + V(\mathbf{x}) + \kappa|\psi|^2 + \lambda\left(U_{\rm dip} * |\psi|^2\right) - \Omega L_z\right]\psi(\mathbf{x}, t), \tag{1.1}$$

where t denotes time and $\mathbf{x} = (x, y, z)^T \in \mathbb{R}^3$ is the Cartesian coordinate vector. $V(\mathbf{x})$ is a given real-valued external trapping potential which is determined by the type of system under investigation. The constant κ describes the strength of the short-range two-body interactions (positive for repulsive interaction and negative for attractive interaction) in a condensate, and λ describes the strength of the long-range DDI. The constant $\Omega \in \mathbb{R}$ represents the angular velocity, L_z is the z-component of the angular momentum defined as

$$L_z = -i(x\partial_y - y\partial_x), \tag{1.2}$$

and $U_{\rm dip}$ is the long-range DDI potential defined as

$$U_{\rm dip}(\mathbf{x}) = \frac{3}{4\pi|\mathbf{x}|^3}\left[1 - \frac{3(\mathbf{x}\cdot\mathbf{n})^2}{|\mathbf{x}|^2}\right] = \frac{3}{4\pi|\mathbf{x}|^3}\left[1 - 3\cos^2(\vartheta)\right], \qquad \mathbf{x} \in \mathbb{R}^3. \tag{1.3}$$

Here $\mathbf{n} = (n_1, n_2, n_3)^T \in \mathbb{R}^3$ denotes a given unit vector, i.e., $|\mathbf{n}| = \sqrt{n_1^2 + n_2^2 + n_3^2} = 1$, representing the dipole axis (or dipole moment), and $\vartheta = \vartheta_{\mathbf{n}}(\mathbf{x})$ is the angle between the dipole axis $\mathbf{n}$ and the vector $\mathbf{x}$.

Similar to the nonrotating cases in [10, 20], the GPE (1.1) can be reformulated as the following Gross–Pitaevskii–Poisson system:

$$i\partial_t \psi(\mathbf{x}, t) = \left[-\frac{1}{2}\nabla^2 + V(\mathbf{x}) + (\kappa - \lambda)|\psi|^2 - 3\lambda\varphi(\mathbf{x}, t) - \Omega L_z\right]\psi(\mathbf{x}, t), \tag{1.4}$$

$$\varphi(\mathbf{x}, t) = \partial_{\mathbf{nn}} u(\mathbf{x}, t), \quad -\nabla^2 u(\mathbf{x}, t) = |\psi(\mathbf{x}, t)|^2 \ \text{ with } \lim_{|\mathbf{x}|\to\infty} u(\mathbf{x}, t) = 0, \tag{1.5}$$

where $\partial_{\mathbf{n}} = \mathbf{n}\cdot\nabla$ and $\partial_{\mathbf{nn}} = \partial_{\mathbf{n}}(\partial_{\mathbf{n}})$. In some experiments of rotating BECs, the external trap is strongly confined in the z-direction, i.e.,

$$V(\mathbf{x}) = V_2(x, y) + \frac{z^2}{2\varepsilon^4}, \qquad \mathbf{x} \in \mathbb{R}^3, \tag{1.6}$$

with $0 < \varepsilon \ll 1$ a given dimensionless parameter, resulting in a pancake-shaped BEC [7]. In this case, the GPE (1.1) or (1.4)–(1.5) can be approximated by an effective two-dimensional (2D) GPE which is usually called the *surface adiabatic model* (SAM) [10, 20]. Furthermore, the SAM reduces to the *surface density model* (SDM) if we let $\varepsilon \to 0^+$ in the interaction kernel of the SAM [10, 20]. For the detailed derivation of SAM and SDM, see Appendix B in [20].

In the following, we write the 2D and 3D GPE in a unified way in d-dimensions ($d = 2$ or 3) with $\mathbf{x} = (x, y)^T$ when $d = 2$ and $\mathbf{x} = (x, y, z)^T$ when $d = 3$:

$$i\partial_t \psi(\mathbf{x}, t) = \left[-\frac{1}{2}\nabla^2 + V(\mathbf{x}) + \beta|\psi|^2 + \eta\varphi(\mathbf{x}, t) - \Omega L_z\right]\psi(\mathbf{x}, t), \tag{1.7}$$

$$\varphi(\mathbf{x}, t) = L_{\mathbf{n}} u(\mathbf{x}, t), \qquad u(\mathbf{x}, t) = G * |\psi|^2, \qquad \mathbf{x} \in \mathbb{R}^d, \quad t \geq 0, \tag{1.8}$$

where $V(\mathbf{x}) = V_2(x, y)$ comes from (1.6) when $d = 2$, and

$$\beta = \begin{cases} \frac{\kappa+\lambda(3n_3^2-1)}{\varepsilon\sqrt{2\pi}}, \\ \kappa - \lambda, \end{cases} \qquad \eta = \begin{cases} -3\lambda/2, \\ -3\lambda, \end{cases} \qquad L_{\mathbf{n}} = \begin{cases} \partial_{\mathbf{n}_\perp \mathbf{n}_\perp} - n_3^2\nabla^2, & d = 2, \\ \partial_{\mathbf{nn}}, & d = 3, \end{cases} \tag{1.9}$$

with $\mathbf{n}_\perp = (n_1, n_2)^T$. In (1.8), the kernel function is given by

$$G(\mathbf{x}) = \begin{cases} 1/(2\pi|\mathbf{x}|), \\ \frac{1}{(2\pi)^{3/2}} \int_{\mathbb{R}} \frac{e^{-s^2/2}}{\sqrt{|\mathbf{x}|^2+\varepsilon^2 s^2}} ds, \\ 1/(4\pi|\mathbf{x}|), \end{cases} \iff \widehat{G}(\xi) = \begin{cases} 1/|\xi|, & d = 2\,\&\,\text{SDM}, \\ \frac{1}{2\pi^2} \int_{\mathbb{R}} \frac{e^{-\varepsilon^2 s^2/2}}{|\xi|^2+s^2} ds, & d = 2\,\&\,\text{SAM}, \\ 1/|\xi|^2, & d = 3, \end{cases} \tag{1.10}$$

where $\widehat{f}(\xi)$ denotes the Fourier transform of the function $f(\mathbf{x})$ for $\mathbf{x}$, $\xi \in \mathbb{R}^d$. Note that even for the SDM we retain ε-dependence in (1.7) via the parameter β. The initial condition of (1.7)–(1.8) is

$$\psi(\mathbf{x}, 0) = \psi_0(\mathbf{x}), \qquad \mathbf{x} \in \mathbb{R}^d, \qquad \text{such that} \quad \|\psi_0\|^2 := \int_{\mathbb{R}^d} |\psi_0(\mathbf{x})|^2 \, d\mathbf{x} = 1. \tag{1.11}$$

We remark here that in most BEC experiments, the condensate is confined by a harmonic potential, i.e.,

$$V(\mathbf{x}) = \frac{1}{2} \begin{cases} \gamma_x^2 x^2 + \gamma_y^2 y^2, & d = 2, \\ \gamma_x^2 x^2 + \gamma_y^2 y^2 + \gamma_z^2 z^2, & d = 3, \end{cases} \tag{1.12}$$

where $\gamma_x > 0$, $\gamma_y > 0$, and $\gamma_z > 0$ are dimensionless constants proportional to the trapping frequencies in the x-, y-, and z-directions, respectively.

Many numerical methods have been proposed to study the dynamics of nonrotating BECs without DDI, i.e., when $\Omega = 0$ and $\eta = 0$ [5,8,12,15,21,38,45]. Among them, the time-splitting sine/Fourier pseudospectral method is one of the most successful methods. Compared to other methods, the time-splitting pseudospectral method has accuracy of spectral order in space and is easy to implement. In addition, as shown in [10], this method is easily generalized to study the dynamics of dipolar BECs when $\eta \neq 0$. However, when $\Omega \neq 0$, we cannot directly apply the time-splitting pseudospectral method proposed in [8, 12, 15] to study the dynamics of rotating BEC due to the appearance of an angular rotational term which has *non*constant coefficients in $\mathbf{x}$. So far, several pseudospectral type methods have been introduced to solve the GPE with an angular momentum rotation term. For example, a pseudospectral type method was proposed in [11] by reformulating the problem in 2D polar coordinates (r, θ) or 3D cylindrical coordinates (r, θ, z). The method is of second- or fourth-order accuracy in the radial direction and spectral-order accuracy in other directions. A time-splitting alternating direction implicit (TSADI) method was proposed in [14], in which the angular rotation term was split into two parts and the Fourier pseudospectral method was applied for spatial derivatives. In [13], a generalized Laguerre–Fourier–Hermite pseudospectral method was presented in polar/cylindrical coordinates, which has spectral order of accuracy in all spatial directions. These methods have higher spatial accuracy compared to the finite difference/element methods in [3, 9, 29] and are also valid in dissipative variants of the GPE (1.1); cf. [46]. On the other hand, the implementation of these methods can become quite involved. The aim of this paper is to propose a simple and efficient numerical method to solve the GPE in a rotating frame, which may include a dipolar interaction term. One novel idea of the proposed

method consists in the use of rotating Lagrangian coordinates as in [6], in which the angular momentum rotation term vanishes. Hence, we can easily apply the methods for nonrotating BECs in [8, 12, 15] to solve the rotating case.

This paper is organized as follows. In section 2, we present the dynamical laws of rotating dipolar BECs based on the GPE (1.7)–(1.11). Then in section 3, we introduce rotating coordinates and cast the GPE and its dynamical quantities in the new coordinate system. Numerical methods are proposed in section 4 to discretize the GPE for both 2D and 3D cases. In section 5, we compare our method with those in the literature and present some numerical results. We make some concluding remarks in section 6.

2. Dynamical properties. In this section, we recall some main quantities in the study of dynamics of rotating dipolar BECs, including mass, energy, angular momentum expectation, condensate width, and center of mass. The dynamical laws of these quantities are briefly presented and can be used as benchmarks for testing our numerical methods. The detailed proof can be found in [44].

Mass and energy. The GPE in (1.7)–(1.11) has two important invariants: the *mass* (or *normalization*) of the wave function, which is defined as [8, 44]

$$N(t) := \|\psi(\cdot,t)\|^2 := \int_{\mathbb{R}^d} |\psi(\mathbf{x},t)|^2 d\mathbf{x} \equiv \int_{\mathbb{R}^d} |\psi(\mathbf{x},0)|^2 d\mathbf{x} = 1, \qquad t \geq 0, \tag{2.1}$$

and the *energy per particle*

$$\begin{aligned} E(t) := E(\psi(\cdot,t)) &= \int_{\mathbb{R}^d} \left[\frac{1}{2}|\nabla\psi|^2 + V(\mathbf{x})|\psi|^2 + \frac{\beta}{2}|\psi|^4 + \frac{\eta}{2}\varphi|\psi|^2 - \Omega \mathrm{Re}\left(\psi^* L_z \psi\right) \right] d\mathbf{x} \\ &\equiv E(\psi(\cdot,0)) = E(\psi_0), \qquad t \geq 0, \end{aligned} \tag{2.2}$$

where f^*, $\mathrm{Re}(f)$, and $\mathrm{Im}(f)$ denote the conjugate, real part, and imaginary part of the complex-valued function f, respectively.

Angular momentum expectation. The *angular momentum expectation* of a condensate is defined as [11, 15]

$$\langle L_z \rangle(t) = \int_{\mathbb{R}^d} \psi^*(\mathbf{x},t) L_z \psi(\mathbf{x},t)\, d\mathbf{x}, \qquad t \geq 0, \tag{2.3}$$

which usually can be used to measure the vortex flux. For the GPE (1.7)–(1.11) with harmonic potential (1.12), the dynamics of angular momentum expectation is governed by the following ordinary differential equation (ODE) [44]:

$$\frac{d\langle L_z \rangle(t)}{dt} = (\gamma_x^2 - \gamma_y^2) \int_{\mathbb{R}^d} xy|\psi|^2 d\mathbf{x} - \eta \int_{\mathbb{R}^d} |\psi|^2 \left[(x\partial_y - y\partial_x)\varphi \right] d\mathbf{x}, \quad t \geq 0, \tag{2.4}$$

which implies that the angular momentum expectation is conserved, i.e.,

$$\langle L_z \rangle(t) \equiv \langle L_z \rangle(0), \quad t \geq 0, \tag{2.5}$$

when $\gamma_x = \gamma_y$ and $\eta = 0$. Furthermore, when $\eta \neq 0$, if $\gamma_x = \gamma_y$, the angular momentum expectation is still conserved, provided that (i) the dipole axis is parallel

to the z-axis, i.e., $\mathbf{n} = (0,0,1)^T$, and (ii) the initial data is radially/cylindrically symmetric or of central vortex type, i.e., $\psi_0(\mathbf{x}) = f(r)e^{im\theta}$ in two dimensions or $\psi_0(\mathbf{x}) = f(r,z)e^{im\theta}$ in three dimensions with $m \in \mathbb{Z}$ and f a real-valued function.

Condensate width. The *condensate width* in the α-direction (where $\alpha = x, y, z$ or $r = \sqrt{x^2+y^2}$) is defined as [11, 15]

$$\sigma_\alpha(t) = \sqrt{\delta_\alpha(t)}, \quad t \geq 0, \qquad \text{where} \quad \delta_\alpha(t) = \int_{\mathbb{R}^d} \alpha^2 |\psi(\mathbf{x},t)|^2 d\mathbf{x}. \tag{2.6}$$

For a 2D BEC without DDI, if the external trap in (1.12) is radially symmetric, i.e., $\eta = 0$ and $\gamma_x = \gamma_y =: \gamma_r$, then for any initial datum $\psi_0(\mathbf{x})$ in (1.11), we have that

$$\delta_r(t) = \frac{E(\psi_0) + \Omega\langle L_z\rangle(0)}{\gamma_r^2}[1 - \cos(2\gamma_r t)] + \delta_r^{(0)}\cos(2\gamma_r t) + \frac{\delta_r^{(1)}}{2\gamma_r}\sin(2\gamma_r t), \tag{2.7}$$

where $\delta_r(t) := \delta_x(t) + \delta_y(t)$, $\delta_r^{(0)} := \delta_x(0) + \delta_y(0) = \int_{\mathbb{R}^2}(x^2+y^2)|\psi_0|^2 d\mathbf{x}$, and $\delta_r^{(1)} := \dot\delta_x(0) + \dot\delta_y(0) = \int_{\mathbb{R}^2} \mathrm{Im}(\psi_0^* \mathbf{x}\cdot\nabla\psi_0) d\mathbf{x}$ [8,11]. Furthermore, if the initial condition $\psi_0(\mathbf{x})$ is radially symmetric, we have that [8, 11]

$$\delta_x(t) = \delta_y(t) \;=\; \frac{1}{2}\delta_r(t), \quad t \geq 0, \tag{2.8}$$

which implies that the condensate widths $\sigma_x(t) = \sigma_y(t)$ are also periodic functions.

Center of mass. The *center of mass* of a condensate is defined as [11]

$$\mathbf{x}_c(t) = \int_{\mathbb{R}^d} \mathbf{x}\,|\psi(\mathbf{x},t)|^2 d\mathbf{x}, \qquad t \geq 0. \tag{2.9}$$

For the GPE (1.7)–(1.11) with a harmonic potential (1.12), the dynamics of the center of mass satisfies the following second-order ODEs [44]:

$$\ddot{\mathbf{x}}_c(t) - 2\Omega J\dot{\mathbf{x}}_c(t) + (\Lambda + \Omega^2 J^2)\,\mathbf{x}_c(t) = \mathbf{0}, \qquad t \geq 0, \tag{2.10}$$

$$\mathbf{x}_c(0) = \int_{\mathbb{R}^d} \mathbf{x}|\psi_0|^2 d\mathbf{x}, \quad \dot{\mathbf{x}}_c(0) = \int_{\mathbb{R}^d} \mathrm{Im}\,(\psi_0^*\nabla\psi_0)\,d\mathbf{x} - \Omega J\mathbf{x}_c^{(0)}, \tag{2.11}$$

where

$$J = \begin{pmatrix} 0 & 1 \\ -1 & 0 \end{pmatrix}, \qquad \Lambda = \begin{pmatrix} \gamma_x^2 & 0 \\ 0 & \gamma_y^2 \end{pmatrix} \qquad \text{for} \quad d = 2 \tag{2.12}$$

or

$$J = \begin{pmatrix} 0 & 1 & 0 \\ -1 & 0 & 0 \\ 0 & 0 & 0 \end{pmatrix}, \qquad \Lambda = \begin{pmatrix} \gamma_x^2 & 0 & 0 \\ 0 & \gamma_y^2 & 0 \\ 0 & 0 & \gamma_z^2 \end{pmatrix} \qquad \text{for} \quad d = 3. \tag{2.13}$$

This shows that the dynamics of the center of mass depends on the trapping frequencies and the angular velocity, but it is independent of the interaction strength constants β and η in (1.7). The second-order ODEs (2.10)–(2.11) could be further solved analytically; see [53] for details.

An analytical solution under special initial data. An interesting application of the dynamical law (2.10) for the center of mass is that in some circumstances we can construct an analytical solution to the GPE (1.7)–(1.11). Precisely speaking, suppose the initial condition $\psi_0(\mathbf{x})$ in (1.11) is chosen as

$$\psi_0(\mathbf{x}) = \phi_s(\mathbf{x} - \mathbf{x}^0), \qquad \mathbf{x} \in \mathbb{R}^d, \tag{2.14}$$

where $\mathbf{x}^0 \in \mathbb{R}^d$ is a given point and $\phi_s(\mathbf{x})$ is a stationary state of the GPE (1.7), which satisfies the time-independent GPE

$$\mu_s \phi_s(\mathbf{x}) = \left[-\frac{1}{2}\nabla^2 + V(\mathbf{x}) + \beta|\phi_s|^2 + \eta\varphi_s - \Omega L_z \right] \phi_s(\mathbf{x}), \qquad \mathbf{x} \in \mathbb{R}^d, \tag{2.15}$$

$$\varphi_s(\mathbf{x}) = L_{\mathbf{n}} u_s(\mathbf{x}), \qquad u_s(\mathbf{x}) = G * |\phi_s|^2, \qquad \mathbf{x} \in \mathbb{R}^d, \tag{2.16}$$

under the constraint

$$\|\phi_s\|^2 = \int_{\mathbb{R}^d} |\phi_s(\mathbf{x})|^2 d\mathbf{x} = 1 \tag{2.17}$$

with $\mu_s \in \mathbb{R}$ the chemical potential. Under the initial condition (2.14), the exact solution of the GPE (1.7)–(1.11) with harmonic potential (1.12) can be constructed as [11, 44]

$$\psi(\mathbf{x}, t) = \phi_s(\mathbf{x} - \mathbf{x}_c(t))\, e^{-i\mu_s t}\, e^{iw(\mathbf{x},t)}, \qquad \mathbf{x} \in \mathbb{R}^d, \quad t \geq 0, \tag{2.18}$$

where $\mathbf{x}_c(t)$ satisfies the ODE (2.10) with

$$\mathbf{x}_c(0) = \mathbf{x}^0, \qquad \dot{\mathbf{x}}_c(0) = -\Omega J \mathbf{x}^0, \tag{2.19}$$

and $w(\mathbf{x}, t)$ is linear in $\mathbf{x}$, i.e.,

$$w(\mathbf{x}, t) = \mathbf{c}(t) \cdot \mathbf{x} + g(t), \quad \mathbf{c}(t) = (c_1(t), \ldots, c_d(t))^T, \quad \mathbf{x} \in \mathbb{R}^d, \quad t \geq 0,$$

for some functions $\mathbf{c}(t)$ and $g(t)$. Thus, up to phase shifts, ψ remains a stationary state with shifted center at all times.

3. GPE under rotating Lagrangian coordinates.

In this section, we first introduce a coordinate transformation and derive the GPE in the transformed coordinates. Then we reformulate the dynamical quantities presented in section 2 in the new coordinate system.

3.1. A rotating Lagrangian coordinate transformation.

For any time $t \geq 0$, let $A(t)$ be an orthogonal rotational matrix defined as

$$A(t) = \begin{pmatrix} \cos(\Omega t) & \sin(\Omega t) \\ -\sin(\Omega t) & \cos(\Omega t) \end{pmatrix} \qquad \text{if} \quad d = 2 \tag{3.1}$$

and

$$A(t) = \begin{pmatrix} \cos(\Omega t) & \sin(\Omega t) & 0 \\ -\sin(\Omega t) & \cos(\Omega t) & 0 \\ 0 & 0 & 1 \end{pmatrix} \qquad \text{if} \quad d = 3. \tag{3.2}$$

It is easy to verify that $A^{-1}(t) = A^T(t)$ for any $t \geq 0$ and $A(0) = I$ with I the identity matrix. For any $t \geq 0$, we introduce the *rotating Lagrangian coordinates* $\widetilde{\mathbf{x}}$ as [6,24,28]

$$\widetilde{\mathbf{x}} = A^{-1}(t)\mathbf{x} = A^T(t)\mathbf{x} \quad \Leftrightarrow \quad \mathbf{x} = A(t)\widetilde{\mathbf{x}}, \qquad \mathbf{x} \in \mathbb{R}^d, \tag{3.3}$$

and denote the wave function in the new coordinates as $\phi := \phi(\widetilde{\mathbf{x}}, t)$

$$\phi(\widetilde{\mathbf{x}}, t) := \psi(\mathbf{x}, t) = \psi\left(A(t)\widetilde{\mathbf{x}}, t\right), \qquad \mathbf{x} \in \mathbb{R}^d, \quad t \geq 0. \tag{3.4}$$

Here, we refer the Cartesian coordinates $\mathbf{x}$ as the *Eulerian coordinates* and Figure 3.1 depicts the geometrical relation between the Eulerian coordinates $\mathbf{x}$ and the rotating Lagrangian coordinates $\widetilde{\mathbf{x}}$ for any fixed $t \geq 0$.

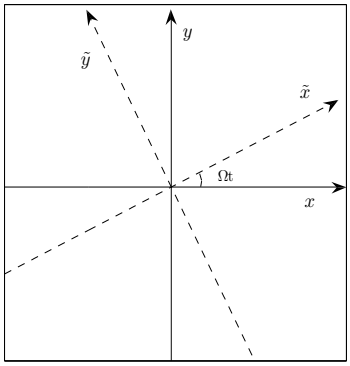

FIG. 3.1. *Cartesian (or Eulerian) coordinates* (x, y) *(solid) and rotating Lagrangian coordinates* $(\tilde{x}, \tilde{y})$ *(dashed) in 2D for any fixed* $t \geq 0$.

Using the chain rule, we obtain the derivatives

$$\begin{aligned}
&\partial_t \phi(\widetilde{\mathbf{x}}, t) = \partial_t \psi(\mathbf{x}, t) + \nabla\psi(\mathbf{x}, t) \cdot \left(\dot{A}(t)\widetilde{\mathbf{x}}\right) = \partial_t \psi(\mathbf{x}, t) - \Omega(x\partial_y - y\partial_x)\psi(\mathbf{x}, t), \\
&\nabla\phi(\widetilde{\mathbf{x}}, t) = A^{-1}(t)\nabla\psi(\mathbf{x}, t), \qquad \nabla^2\phi(\widetilde{\mathbf{x}}, t) = \nabla^2\psi(\mathbf{x}, t).
\end{aligned}$$

Substituting into (1.7)–(1.11) yields the following d-dimensional GPE in the rotating Lagrangian coordinates:

$$i\partial_t \phi(\widetilde{\mathbf{x}}, t) = \left[-\frac{1}{2}\nabla^2 + W(\widetilde{\mathbf{x}}, t) + \beta|\phi|^2 + \eta\varphi(\widetilde{\mathbf{x}}, t)\right]\phi(\widetilde{\mathbf{x}}, t), \quad \widetilde{\mathbf{x}} \in \mathbb{R}^d, \quad t > 0, \tag{3.5}$$

$$\varphi(\widetilde{\mathbf{x}}, t) = L_{\mathbf{m}(t)} u(\widetilde{\mathbf{x}}, t), \qquad u(\widetilde{\mathbf{x}}, t) = G * |\phi|^2, \qquad \widetilde{\mathbf{x}} \in \mathbb{R}^d, \quad t \geq 0, \tag{3.6}$$

where G is defined in (1.10) and

$$W(\widetilde{\mathbf{x}}, t) = V(A(t)\widetilde{\mathbf{x}}), \qquad \widetilde{\mathbf{x}} \in \mathbb{R}^d, \tag{3.7}$$

$$L_{\mathbf{m}(t)} = \begin{cases} \partial_{\mathbf{m}_\perp(t)\mathbf{m}_\perp(t)} - n_3^2\nabla^2, & d = 2, \\ \partial_{\mathbf{m}(t)\mathbf{m}(t)}, & d = 3, \end{cases} \qquad t \geq 0, \tag{3.8}$$

with $\mathbf{m}(t) \in \mathbb{R}^3$ defined as

$$\mathbf{m}(t) = \begin{pmatrix} m_1(t) \\ m_2(t) \\ m_3(t) \end{pmatrix} := A^{-1}(t)\mathbf{n} = \begin{pmatrix} n_1\cos(\Omega t) - n_2\sin(\Omega t) \\ n_1\sin(\Omega t) + n_2\cos(\Omega t) \\ n_3 \end{pmatrix}, \quad t \geq 0, \tag{3.9}$$

and $\mathbf{m}_\perp(t) = (m_1(t), m_2(t))^T$. The initial data of (3.5) is

$$\phi(\widetilde{\mathbf{x}}, 0) = \psi(\mathbf{x}, 0) = \psi_0(\mathbf{x}) := \phi_0(\mathbf{x}) = \phi_0(\widetilde{\mathbf{x}}), \qquad \widetilde{\mathbf{x}} = \mathbf{x} \in \mathbb{R}^d. \tag{3.10}$$

We remark here that if $V(\mathbf{x})$ in (1.7) is a harmonic potential as defined in (1.12), then the potential $W(\widetilde{\mathbf{x}},t)$ in (3.7) has the form

$$W(\widetilde{\mathbf{x}},t)=\frac{1}{4}\begin{cases}\omega_1(\widetilde{x}^2+\widetilde{y}^2)+\omega_2\left[(\widetilde{x}^2-\widetilde{y}^2)\cos(2\Omega t)+2\widetilde{x}\widetilde{y}\sin(2\Omega t)\right], & d=2,\\ \omega_1(\widetilde{x}^2+\widetilde{y}^2)+\omega_2\left[(\widetilde{x}^2-\widetilde{y}^2)\cos(2\Omega t)+2\widetilde{x}\widetilde{y}\sin(2\Omega t)\right]+2\gamma_z^2\widetilde{z}^2, & d=3,\end{cases}$$

where $\omega_1=\gamma_x^2+\gamma_y^2$ and $\omega_2=\gamma_x^2-\gamma_y^2$. It is easy to see that when $\gamma_x=\gamma_y:=\gamma_r$, i.e., radially and cylindrically symmetric harmonic trap in two and three dimensions, respectively, we have $\omega_1=2\gamma_r^2$ and $\omega_2=0$ and thus the potential $W(\widetilde{\mathbf{x}},t)=V(\widetilde{\mathbf{x}})$ becomes time-independent.

In contrast to (1.7), the angular momentum rotation term in GPE (3.5) has vanished and instead the external potential and the dipole axis have become time-dependent. The absence of an angular momentum rotation term in (3.5) enables us to develop simple and efficient numerical methods for simulating the dynamics of rotating dipolar BEC in section 4.

3.2. Dynamical quantities. In section 3.1, we introduced rotating Lagrangian coordinates and cast the GPE in the new coordinate system. Next we consider the dynamical quantities in terms of the new wave function $\phi(\widetilde{\mathbf{x}},t)$.

Conserved quantities. In rotating Lagrangian coordinates, there are two conserved quantities [11, 44], i.e.,

$$\widetilde{N}(t)=\|\phi(\cdot,t)\|^2:=\int_{\mathbb{R}^d}|\phi(\widetilde{\mathbf{x}},t)|^2d\widetilde{\mathbf{x}}=\int_{\mathbb{R}^d}|\psi(\mathbf{x},t)|^2d\mathbf{x}=N(t)\equiv 1,\qquad t\geq 0, \tag{3.11}$$

and

$$\begin{aligned}\widetilde{E}(t):=\widetilde{E}(\phi(\cdot,t))&=\int_{\mathbb{R}^d}\left[\frac{1}{2}|\nabla\phi|^2+W(\widetilde{\mathbf{x}},t)|\phi|^2+\frac{\beta}{2}|\phi|^4+\frac{\eta}{2}\varphi|\phi|^2\right]d\widetilde{\mathbf{x}}\\&\quad-\int_{\mathbb{R}^d}\int_0^t\left[\partial_\tau W(\widetilde{\mathbf{x}},\tau)+\frac{\eta}{2}(\partial_\tau L_{\mathbf{m}(\tau)})u(\widetilde{\mathbf{x}},\tau)\right]|\phi|^2d\tau\,d\widetilde{\mathbf{x}}\\&\equiv\widetilde{E}(\phi(\cdot,0))=\widetilde{E}(\phi_0)=\widetilde{E}(\psi_0)=E(\psi_0)+\Omega\,\langle L_z\rangle(0)\\&\equiv E(\psi(\cdot,t))+\Omega\,\langle L_z\rangle(0)=E(t)+\Omega\,\langle L_z\rangle(0),\qquad t\geq 0,\end{aligned} \tag{3.12}$$

where u is given in (3.6) and

$$\partial_t L_{\mathbf{m}(t)}=2\begin{cases}\partial_{\dot{A}^T(t)\mathbf{n}_\perp}\partial_{A^T(t)\mathbf{n}_\perp}, & d=2,\\ \partial_{\dot{A}^T(t)\mathbf{n}}\partial_{A^T(t)\mathbf{n}}, & d=3,\end{cases}\qquad t\geq 0.$$

Angular momentum expectation. The angular momentum expectation (2.3) in the new coordinates becomes

$$\begin{aligned}\langle L_z\rangle(t)&=-i\int_{\mathbb{R}^d}\psi^*(\mathbf{x},t)(x\partial_y-y\partial_x)\psi(\mathbf{x},t)\,d\mathbf{x}\\&=-i\int_{\mathbb{R}^d}\phi^*(\widetilde{\mathbf{x}},t)(\widetilde{x}\partial_{\tilde{y}}-\widetilde{y}\partial_{\tilde{x}})\phi(\widetilde{\mathbf{x}},t)\,d\widetilde{\mathbf{x}}\\&=\langle L_{\tilde{z}}\rangle(t),\qquad t\geq 0.\end{aligned} \tag{3.13}$$

In addition, combining (2.2), (3.12), (2.3), and (3.13) and noticing (3.3) and (3.4), we get for $\Omega\neq 0$

$$\frac{d\,\langle L_z\rangle(t)}{dt}=\frac{1}{\Omega}\int_{\mathbb{R}^d}\left[\partial_t W(\widetilde{\mathbf{x}},t)+\frac{\eta}{2}(\partial_t L_{\mathbf{m}(t)})u(\widetilde{\mathbf{x}},t)\right]|\phi(\widetilde{\mathbf{x}},t)|^2d\widetilde{\mathbf{x}},\qquad t\geq 0. \tag{3.14}$$

Condensate width. After the coordinate transform, we have that

$$\delta_r(t) = \int_{\mathbb{R}^d} (x^2+y^2)|\psi|^2 d\mathbf{x} = \int_{\mathbb{R}^d} (\widetilde{x}^2+\widetilde{y}^2)|\phi|^2 d\widetilde{\mathbf{x}} = \delta_{\tilde{x}}(t) + \delta_{\tilde{y}}(t), \tag{3.15}$$

$$\delta_z(t) = \int_{\mathbb{R}^d} z^2|\psi|^2 d\mathbf{x} = \int_{\mathbb{R}^d} \widetilde{z}^2|\phi|^2 d\widetilde{\mathbf{x}} = \delta_{\tilde{z}}(t) \tag{3.16}$$

for any $t \geq 0$.

Center of mass. The center of mass in rotating Lagrangian coordinates is

$$\widetilde{\mathbf{x}}_c(t) = \int_{\mathbb{R}^d} \widetilde{\mathbf{x}}\, |\phi(\widetilde{\mathbf{x}},t)|^2 d\widetilde{\mathbf{x}}, \qquad t \geq 0. \tag{3.17}$$

Since $\det(A(t)) = 1$ for any $t \geq 0$, it holds that $\mathbf{x}_c(t) = A(t)\widetilde{\mathbf{x}}_c(t)$ for any time $t \geq 0$. Using $\dot{A}(t)^T = -\Omega J A(t)^T$, it is easy to see that the ODE (2.10) in rotating coordinates turns into

$$\ddot{\widetilde{\mathbf{x}}}_c(t) + A^T(t)\Lambda A(t)\,\widetilde{\mathbf{x}}_c(t) = \mathbf{0}, \qquad t \geq 0, \tag{3.18}$$

where the matrix Λ is defined in (2.12) and (2.13) for two and three dimensions, respectively. In the rotating Lagrangian coordinates, the special solution (2.18) with initial datum

$$\phi_0(\widetilde{\mathbf{x}}) = \phi_s(\widetilde{\mathbf{x}} - \widetilde{\mathbf{x}}^0), \qquad \widetilde{\mathbf{x}} \in \mathbb{R}^d, \tag{3.19}$$

is transformed to

$$\phi(\widetilde{\mathbf{x}},t) = \phi_s(\widetilde{\mathbf{x}} - \widetilde{\mathbf{x}}_c(t))\, e^{-i\mu_s t}\, e^{i\widetilde{w}(\widetilde{\mathbf{x}},t)}, \qquad t > 0, \tag{3.20}$$

where $\widetilde{\mathbf{x}}_c(t)$ satisfies the second-order ODE (3.18) with initial datum given by

$$\widetilde{\mathbf{x}}_c(0) = \widetilde{\mathbf{x}}^0 = \mathbf{x}^0, \qquad \dot{\widetilde{\mathbf{x}}}_c(0) = \mathbf{0}, \tag{3.21}$$

and $\widetilde{w}(\widetilde{\mathbf{x}},t)$ is linear in $\widetilde{\mathbf{x}}$, i.e.,

$$\widetilde{w}(\widetilde{\mathbf{x}},t) = \widetilde{\mathbf{c}}(t)\cdot\widetilde{\mathbf{x}} + \widetilde{g}(t), \quad \widetilde{\mathbf{c}}(t) = (\widetilde{c}_1(t),\ldots,\widetilde{c}_d(t))^T, \quad \mathbf{x} \in \mathbb{R}^d, \quad t \geq 0.$$

In addition, the form of the transformation matrix $A(t)$ in (3.2) implies that the coordinate transformation does not affect the quantities in the z-direction, e.g., $\langle L_z\rangle$, $\sigma_z(t)$ and $z_c(t)$.

4. Numerical methods. To study the dynamics of rotating dipolar BECs, in this section we propose a simple and efficient numerical method for discretizing the GPE (3.5)–(3.10) in rotating Lagrangian coordinates. The detailed discretization for both 2D and 3D GPEs are presented. Here we assume that $\Omega \neq 0$, and for the numerical methods when $\Omega = 0$, we refer to [8, 10, 20, 48].

In practical computations, we first truncate the whole space problem (3.5)–(3.10) into a bounded computational domain $\mathcal{D} \subset \mathbb{R}^d$ and consider

$$i\partial_t\phi(\widetilde{\mathbf{x}},t) = -\frac{1}{2}\nabla^2\phi + W(\widetilde{\mathbf{x}},t)\phi + \beta|\phi|^2\phi + \eta\varphi\phi, \quad \widetilde{\mathbf{x}} \in \mathcal{D}, \quad t > 0, \tag{4.1}$$

$$\varphi(\widetilde{\mathbf{x}},t) = L_{\mathbf{m}(t)}u(\widetilde{\mathbf{x}},t), \quad u(\widetilde{\mathbf{x}},t) = \int_{\mathbb{R}^d} G(\widetilde{\mathbf{x}}-\widetilde{\mathbf{y}})\rho(\widetilde{\mathbf{y}},t)\, d\widetilde{\mathbf{y}}, \quad \widetilde{\mathbf{x}} \in \mathcal{D}, \quad t > 0, \tag{4.2}$$

where

$$\rho(\widetilde{\mathbf{y}},t)=\begin{cases}|\phi(\widetilde{\mathbf{y}},t)|^2, & \widetilde{\mathbf{y}}\in\mathcal{D},\\ 0, & \widetilde{\mathbf{y}}\in\mathbb{R}^d\backslash\mathcal{D}.\end{cases}$$

The initial condition is

$$\phi(\widetilde{\mathbf{x}},0)=\phi_0(\widetilde{\mathbf{x}}),\qquad \widetilde{\mathbf{x}}\in\overline{\mathcal{D}}. \tag{4.3}$$

The computational domain $\mathcal{D}\subset\mathbb{R}^d$ is chosen as $\mathcal{D}=[a,b]\times[c,d]$ if $d=2$ and $\mathcal{D}=[a,b]\times[c,d]\times[e,f]$ if $d=3$. Due to the confinement of the external potential, the wave function decays exponentially fast as $|\widetilde{\mathbf{x}}|\to\infty$. Thus if we choose $\mathcal{D}$ to be sufficiently large, the errors from the domain truncation can be neglected. After we solve $\phi(\widetilde{\mathbf{x}},t)$ in the bounded computational domain $\mathcal{D}$, a corresponding solution $\psi(\mathbf{x},t)$ in the domain $A(t)\mathcal{D}$ can be obtained. As shown in Figure 4.1 for the example of a 2D domain, although the domains $A(t)\mathcal{D}$ for $t\geq 0$ are in general different for different time t, they share a common disk which is bounded by the inner green circle in Figure 4.1. Thus, the value of $\psi(\mathbf{x},t)$ inside the vertical maximal square (the shaded area) which lies fully within the inner disk can be calculated easily by interpolation.

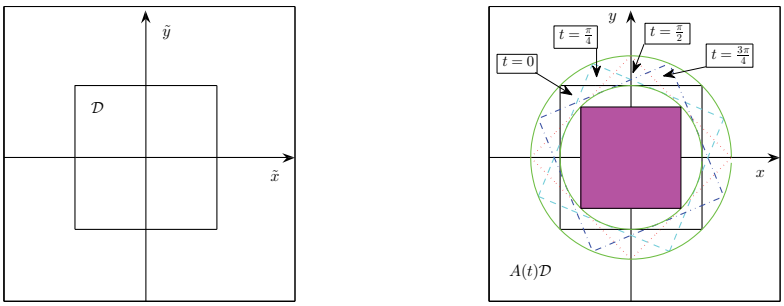

FIG. 4.1. *The bounded computational domain $\mathcal{D}$ in rotating Lagrangian coordinates $\widetilde{\mathbf{x}}$ (left) and the corresponding domain $A(t)\mathcal{D}$ in Cartesian (or Eulerian) coordinates $\mathbf{x}$ (right) when $\Omega=0.5$ at different times: $t=0$ (black solid), $t=\frac{\pi}{4}$ (cyan dashed), $t=\frac{\pi}{2}$ (red dotted), and $t=\frac{3\pi}{4}$ (blue dash-dotted). The two green circles determine two disks which are the union (outer circle) and the intersection (inner circle) of all domains $A(t)\mathcal{D}$ for $t\geq 0$, respectively. The magenta (shaded) area is the vertical maximal square inside the inner circle.*

The boundary conditions of (4.1) will be chosen based on the kernel function G defined in (1.10). Due to the convolution in (4.2), it is natural to consider using the Fourier transform to compute $u(\widetilde{\mathbf{x}},t)$. However, as noted for simulating dipolar BECs in three dimensions [10, 16, 40], there is a numerical locking phenomenon, i.e., numerical errors will be bounded below no matter how small the mesh size is, when one uses the Fourier transform to evaluate $u(\widetilde{\mathbf{x}},t)$ and/or $\varphi(\widetilde{\mathbf{x}},t)$ numerically in (4.2). This is because $\lim_{\xi\to 0}\widehat{G}(\xi)=\infty$ and $\widehat{|\phi|^2}(\xi=0)\neq 0$, which is easily obtained from (1.10) and (3.11). To resolve it, we notice that the second (integral) equation in (4.2) can be reformulated into the Poisson equation (1.5) for the 3D model and square-root-Poisson equation for the 2D SDM model [7, 10]. With these PDE formulations for $u(\widetilde{\mathbf{x}},t)$, we can truncate them on the domain $\mathcal{D}$ and solve them numerically via a spectral method with sine basis functions instead of Fourier basis functions so as to avoid using the 0-modes [10]. Thus in the 3D and the 2D SDM model, we choose the homogeneous Dirichlet boundary conditions to (4.1). Of course, for the 2D SAM

model, one has to use the Fourier transform to compute $u(\widetilde{\mathbf{x}},t)$, thus we take the periodic boundary conditions to (4.1).

Remark 4.1. Since the Green's function G in all three cases of (1.10) decays like $|\mathbf{x}|^{-1}$, the solution u to (4.2) with ρ supported in the interior of $\mathcal{D}$ effectively satisfies zero Dirichlet boundary conditions. This is true at least as long as the domain $\mathcal{D}$ is chosen large enough compared to the support of ρ. Note that we have already observed that in the presence of the trapping potential W, the density ρ of the wave function indeed decays exponentially within $\mathcal{D}$ when it is chosen large enough.

4.1. Time-splitting method. Next, we introduce a time-splitting method to discretize (4.1)–(4.3). We choose a time step size $\Delta t > 0$ and define the time sequence as $t_n = n\Delta t$ for $n = 0, 1, \ldots$. Then from $t = t_n$ to $t = t_{n+1}$, we numerically solve the GPE (4.1) in two steps. First we solve

$$i\partial_t \phi(\widetilde{\mathbf{x}},t) = -\frac{1}{2}\nabla^2 \phi(\widetilde{\mathbf{x}},t), \quad \widetilde{\mathbf{x}} \in \mathcal{D}, \quad t_n \le t \le t_{n+1}, \tag{4.4}$$

for a time step of length Δt, and then we solve

$$i\partial_t \phi(\widetilde{\mathbf{x}},t) = \left[W(\widetilde{\mathbf{x}},t) + \beta|\phi|^2 + \eta\varphi\right]\phi(\widetilde{\mathbf{x}},t), \quad \widetilde{\mathbf{x}} \in \mathcal{D}, \quad t_n \le t \le t_{n+1}, \tag{4.5}$$

$$\varphi(\widetilde{\mathbf{x}},t) = L_{\mathbf{m}(t)} u(\widetilde{\mathbf{x}},t), \qquad u(\widetilde{\mathbf{x}},t) = \int_{\mathbb{R}^d} G(\widetilde{\mathbf{x}}-\widetilde{\mathbf{y}})\rho(\widetilde{\mathbf{y}},t)\, d\widetilde{\mathbf{y}}, \tag{4.6}$$

for the same time step.

Equation (4.4) can be discretized in space by sine or Fourier pseudospectral methods and then integrated exactly in time. If homogeneous Dirichlet boundary conditions are used, then we choose the sine pseudospectral method to discretize it; otherwise, the Fourier pseudospectral method is used if the boundary conditions are periodic. For more details, see, e.g., [8, 10, 12, 15].

On the other hand, we notice that on each time interval $[t_n, t_{n+1}]$, the problem (4.5)–(4.6) leaves $|\phi(\widetilde{\mathbf{x}},t)|$ and hence $u(\widetilde{\mathbf{x}},t)$ invariant, i.e., $|\phi(\widetilde{\mathbf{x}},t)| = |\phi(\widetilde{\mathbf{x}},t_n)|$ and $u(\widetilde{\mathbf{x}},t) = u(\widetilde{\mathbf{x}},t_n)$ for any time $t_n \le t \le t_{n+1}$. Thus, for $t \in [t_n, t_{n+1}]$, (4.5) reduces to

$$i\partial_t \phi(\widetilde{\mathbf{x}},t) = \left[W(\widetilde{\mathbf{x}},t) + \beta|\phi(\widetilde{\mathbf{x}},t_n)|^2 + \eta\left(L_{\mathbf{m}(t)}u(\widetilde{\mathbf{x}},t_n)\right)\right]\phi(\widetilde{\mathbf{x}},t), \quad \widetilde{\mathbf{x}} \in \mathcal{D}. \tag{4.7}$$

Integrating (4.7) in time gives the solution

$$\phi(\widetilde{\mathbf{x}},t) = \phi(\widetilde{\mathbf{x}},t_n)\exp\left[-i\left(\beta|\phi(\widetilde{\mathbf{x}},t_n)|^2(t-t_n) + \eta\Phi(\widetilde{\mathbf{x}},t) + \int_{t_n}^{t} W(\widetilde{\mathbf{x}},\tau)d\tau\right)\right] \tag{4.8}$$

for $\widetilde{\mathbf{x}} \in \mathcal{D}$ and $t \in [t_n, t_{n+1}]$, where the function $\Phi(\widetilde{\mathbf{x}},t)$ is defined by

$$\Phi(\widetilde{\mathbf{x}},t) = \int_{t_n}^{t}\left[L_{\mathbf{m}(\tau)}u(\widetilde{\mathbf{x}},t_n)\right]d\tau = \left(\int_{t_n}^{t} L_{\mathbf{m}(\tau)}\, d\tau\right)u(\widetilde{\mathbf{x}},t_n). \tag{4.9}$$

Plugging (3.9) and (3.8) into (4.9), we get

$$\Phi(\widetilde{\mathbf{x}},t) = \tilde{L}_d(t)u(\widetilde{\mathbf{x}},t_n), \qquad \widetilde{\mathbf{x}} \in \mathcal{D}, \quad t_n \le t \le t_{n+1}, \tag{4.10}$$

where

$$\tilde{L}_d(t) = \begin{cases} [l_e^{11}(t) - l_e^{33}(t)]\partial_{\tilde{x}\tilde{x}} + [l_e^{22}(t) - l_e^{33}(t)]\partial_{\tilde{y}\tilde{y}} + l_e^{12}(t)\partial_{\tilde{x}\tilde{y}}, & d = 2, \\ l_e^{11}(t)\partial_{\tilde{x}\tilde{x}} + l_e^{22}(t)\partial_{\tilde{y}\tilde{y}} + l_e^{33}(t)\partial_{\tilde{z}\tilde{z}} + l_e^{12}(t)\partial_{\tilde{x}\tilde{y}} + l_e^{13}(t)\partial_{\tilde{x}\tilde{z}} + l_e^{23}(t)\partial_{\tilde{y}\tilde{z}}, & d = 3, \end{cases}$$

with

$$
\begin{aligned}
l_e^{11}(t) &= \int_{t_n}^{t} m_1^2(\tau)d\tau = \int_{t_n}^{t} \left[n_1^2\cos^2(\Omega\tau) + n_2^2\sin^2(\Omega\tau) - n_1n_2\sin(2\Omega\tau)\right] d\tau \\
&= \frac{n_1^2+n_2^2}{2}(t-t_n) + \frac{n_1^2-n_2^2}{4\Omega}\left[\sin(2\Omega t) - \sin(2\Omega t_n)\right] + \frac{n_1n_2}{2\Omega}\left[\cos(2\Omega t)\right. \\
&\quad \left. - \cos(2\Omega t_n)\right], \\
l_e^{22}(t) &= \int_{t_n}^{t} m_2^2(\tau)d\tau = \int_{t_n}^{t} \left[n_2^2\cos^2(\Omega\tau) + n_1^2\sin^2(\Omega\tau) + n_1n_2\sin(2\Omega\tau)\right] d\tau \\
&= \frac{n_1^2+n_2^2}{2}(t-t_n) - \frac{n_1^2-n_2^2}{4\Omega}\left[\sin(2\Omega t) - \sin(2\Omega t_n)\right] - \frac{n_1n_2}{2\Omega}\left[\cos(2\Omega t)\right. \\
&\quad \left. - \cos(2\Omega t_n)\right], \\
l_e^{12}(t) &= 2\int_{t_n}^{t} m_1(\tau)m_2(\tau)d\tau = \int_{t_n}^{t} \left[(n_1^2-n_2^2)\sin(2\Omega\tau) + 2n_1n_2\cos(2\Omega t)\right] d\tau \\
&= \frac{n_1^2-n_2^2}{2\Omega}\left[\cos(2\Omega t_n) - \cos(2\Omega t)\right] + \frac{n_1n_2}{\Omega}\left[\sin(2\Omega t) - \sin(2\Omega t_n)\right], \\
l_e^{13}(t) &= 2n_3\int_{t_n}^{t} m_1(\tau)d\tau = 2n_3\int_{t_n}^{t} \left[n_1\cos(\Omega\tau) - n_2\sin(\Omega\tau)\right] d\tau \\
&= \frac{2n_3}{\Omega}\Big[n_1\left[\sin(\Omega t) - \sin(\Omega t_n)\right] + n_2\left[\cos(\Omega t) - \cos(\Omega t_n)\right]\Big], \\
l_e^{23}(t) &= 2n_3\int_{t_n}^{t} m_2(\tau)d\tau = 2n_3\int_{t_n}^{t} \left[n_1\sin(\Omega\tau) + n_2\cos(\Omega\tau)\right] d\tau \\
&= \frac{2n_3}{\Omega}\Big[n_2\left[\sin(\Omega t) - \sin(\Omega t_n)\right] - n_1\left[\cos(\Omega t) - \cos(\Omega t_n)\right]\Big], \\
l_e^{33}(t) &= \int_{t_n}^{t} n_3^2\, d\tau = n_3^2(t-t_n), \qquad t_n \le t \le t_{n+1}.
\end{aligned}
$$

In section 4.2, we will discuss in detail the approximations to $\Phi(\widetilde{\mathbf{x}}, t)$ in (4.10). In addition, if $V(\mathbf{x})$ in (1.7) is a harmonic potential as defined in (1.12), then the definite integral in (4.8) can be calculated analytically as

$$
\int_{t_n}^{t} W(\widetilde{\mathbf{x}}, \tau)d\tau = \frac{1}{4}\omega_1(\widetilde{x}^2+\widetilde{y}^2)(t-t_n) + H(\widetilde{\mathbf{x}}, t) + \frac{1}{2}\begin{cases} 0, & d=2, \\ \gamma_z^2\widetilde{z}^2(t-t_n), & d=3, \end{cases}
$$

where

$$
\begin{aligned}
H(\widetilde{\mathbf{x}}, t) &= \frac{1}{4}\int_{t_n}^{t} \omega_2\left[(\widetilde{x}^2-\widetilde{y}^2)\cos(2\Omega\tau) + 2\widetilde{x}\widetilde{y}\sin(2\Omega\tau)\right] d\tau \\
&= \frac{\omega_2}{8\Omega}\left[\left(\widetilde{x}^2-\widetilde{y}^2\right)\left[\sin(2\Omega t) - \sin(2\Omega t_n)\right] - 2\widetilde{x}\widetilde{y}\left[\cos(2\Omega t) - \cos(2\Omega t_n)\right]\right].
\end{aligned}
$$

Of course, for general external potential $V(\mathbf{x})$ in (1.7), the integral of $W(\widetilde{\mathbf{x}}, \tau)$ in (4.8) might not be found analytically. In this situation, we can simply adopt a numerical quadrature to approximate it, e.g., the Simpson's rule can be used,

$$
\int_{t_n}^{t} W(\widetilde{\mathbf{x}}, \tau)\, d\tau \approx \frac{t-t_n}{6}\left[W(\widetilde{\mathbf{x}}, t_n) + 4W\left(\widetilde{\mathbf{x}}, \frac{t_n+t}{2}\right) + W(\widetilde{\mathbf{x}}, t)\right].
$$

In practice, we use the second-order Strang splitting method [43] to combine the two steps in (4.4) and (4.5)–(4.6). That is, from time $t = t_n$ to $t = t_{n+1}$, we (i) solve (4.4) for half time step $\Delta t/2$ with initial data given at $t = t_n$; (ii) solve (4.5)–(4.6) for one step Δt starting with the data obtained from (i); and (iii) solve (4.4) for half time step $\Delta t/2$ again with the data obtained from (ii). For a more general discussion of the split-step method, we refer the readers to [8, 15, 25].

4.2. Computation of $\Phi(\widetilde{\mathbf{x}}, t)$. In this section, we present approximations to the function $\Phi(\widetilde{\mathbf{x}}, t)$ in (4.10). As discussed previously, we will only focus on discretizing $u(\widetilde{\mathbf{x}}, t_n)$ in (4.2) and its second-order derivatives in (4.10).

4.2.1. SAM in two dimensions. In this case, the function $u(\widetilde{\mathbf{x}}, t_n)$ in (4.10) is defined as

$$u(\widetilde{\mathbf{x}}, t_n) = \int_{\mathbb{R}^2} G(\widetilde{\mathbf{x}} - \widetilde{\mathbf{y}})\rho(\widetilde{\mathbf{y}}, t_n)\, d\widetilde{\mathbf{y}}, \qquad \widetilde{\mathbf{x}} \in \mathcal{D}, \tag{4.11}$$

with the kernel function G defined in the second line of (1.10). To approximate it, we consider a 2D box $\mathcal{D}$ with periodic boundary conditions.

Let M and K be two even positive integers. We make the (approximate) ansatz

$$u(\widetilde{\mathbf{x}}, t_n) = \sum_{p=-M/2}^{M/2-1} \sum_{q=-K/2}^{K/2-1} \widehat{u}^f_{pq}(t_n)\, e^{i\nu_p^1(\widetilde{x}-a)} e^{i\nu_q^2(\widetilde{y}-c)}, \qquad \widetilde{\mathbf{x}} = (\widetilde{x}, \widetilde{y}) \in \mathcal{D}, \tag{4.12}$$

where $\widehat{u}^f_{pq}(t_n)$ is the Fourier coefficient of $u(\widetilde{\mathbf{x}}, t_n)$ corresponding to the frequencies (p, q) and

$$\nu_p^1 = \frac{2p\pi}{b-a}, \quad \nu_q^2 = \frac{2q\pi}{d-c}, \qquad (p, q) \in \mathcal{S}_{MK}.$$

The index set $\mathcal{S}_{MK}$ is defined as

$$\mathcal{S}_{MK} = \{(p, q) \,|\, -M/2 \le p \le M/2 - 1,\ -K/2 \le q \le K/2 - 1\}.$$

We approximate the convolution in (4.11) by a discrete convolution and take its discrete Fourier transform to obtain

$$\widehat{u}^f_{pq}(t_n) = \widehat{G}(\nu_p^1, \nu_q^2) \cdot (\widehat{|\phi^n|^2})^f_{pq}, \qquad (p, q) \in \mathcal{S}_{MK}, \tag{4.13}$$

where $(\widehat{|\phi^n|^2})^f_{pq}$ is the Fourier transform coefficient of the function $|\phi(\widetilde{\mathbf{x}}, t_n)|^2$ (or the discrete Fourier transform coefficient when the values of the function $|\phi(\widetilde{\mathbf{x}}, t_n)|^2$ are only available on the grid points of the bounded computational domain $\mathcal{D}$ in practical computations) corresponding to the frequencies (p, q), and $\widehat{G}(\nu_p^1, \nu_q^2)$ are given by (see details in (1.10))

$$\widehat{G}(\nu_p^1, \nu_q^2) = \frac{1}{2\pi^2} \int_{-\infty}^{\infty} \frac{e^{-\varepsilon^2 s^2/2}}{(\nu_p^1)^2 + (\nu_q^2)^2 + s^2} ds, \qquad (p, q) \in \mathcal{S}_{MK}. \tag{4.14}$$

Since the integrand in (4.14) decays exponentially fast, in practice we can first truncate it to an interval $[s_1, s_2]$ with $|s_1|, s_2 > 0$ sufficiently large and then evaluate the truncated integral by using quadrature rules, e.g., composite Simpson's or trapezoidal quadrature rule.

Combining (4.10), (4.12), and (4.13), we obtain an approximation of $\Phi(\widetilde{\mathbf{x}},t)$ in the solution (4.8) via the Fourier spectral method as

$$\Phi(\widetilde{\mathbf{x}},t)=\sum_{p=-M/2}^{M/2-1}\sum_{q=-K/2}^{K/2-1}\left[L(\nu_p^1,\nu_q^2,t)\widehat{G}(\nu_p^1,\nu_q^2)\cdot(\widehat{|\phi^n|^2})_{pq}^f\right]e^{i\nu_p^1(\widetilde{x}-a)}e^{i\nu_q^2(\widetilde{y}-c)} \tag{4.15}$$

for time $t_n\le t\le t_{n+1}$, where the function $L(\xi_1,\xi_2,t)$ is defined as

$$L(\xi_1,\xi_2,t)=-\left[\left(l_e^{11}(t)-l_e^{33}(t)\right)\xi_1^2+\left(l_e^{22}(t)-l_e^{33}(t)\right)\xi_2^2+l_e^{12}(t)\xi_1\xi_2\right].$$

4.2.2. SDM in two dimensions. In this case, the function $u(\widetilde{\mathbf{x}},t_n)$ in (4.10) also satisfies the square-root-Poisson equation [8, 20], which can be truncated on the computational domain $\mathcal{D}$ with homogeneous Dirichlet boundary conditions as

$$(-\nabla^2)^{1/2}u(\widetilde{\mathbf{x}},t_n)=|\phi(\widetilde{\mathbf{x}},t_n)|^2,\quad \widetilde{\mathbf{x}}\in\mathcal{D};\qquad u(\widetilde{\mathbf{x}},t_n)|_{\partial\mathcal{D}}=0. \tag{4.16}$$

The above problem can be discretized by using a sine pseudospectral method in which the 0-modes are avoided. Letting $M,K\in\mathbb{N}$, we denote the index set

$$\mathcal{T}_{MK}=\{(p,q)\,|\,1\le p\le M-1,\ 1\le q\le K-1\}$$

and define the functions

$$U_{p,q}(\widetilde{\mathbf{x}})=\sin(\mu_p^1(\widetilde{x}-a))\sin(\mu_q^2(\widetilde{y}-c)),\qquad (p,q)\in\mathcal{T}_{MK},\quad \widetilde{\mathbf{x}}=(\widetilde{x},\widetilde{y})\in\mathcal{D},$$

where

$$\mu_p^1=\frac{p\pi}{b-a},\qquad \mu_q^2=\frac{q\pi}{d-c},\qquad (p,q)\in\mathcal{T}_{MK}. \tag{4.17}$$

Assume that

$$u(\widetilde{\mathbf{x}},t_n)=\sum_{p=1}^{M-1}\sum_{q=1}^{K-1}\widehat{u}_{pq}^s(t_n)U_{p,q}(\widetilde{\mathbf{x}}),\qquad \widetilde{\mathbf{x}}\in\mathcal{D}, \tag{4.18}$$

where $\widehat{u}_{pq}^s(t_n)$ is the sine transform of $u(\widetilde{\mathbf{x}},t_n)$ at frequencies (p,q). Substituting (4.18) into (4.16) and taking the sine transform on both sides, we obtain

$$\widehat{u}_{pq}^s(t_n)=\frac{(\widehat{|\phi^n|^2})_{pq}^s}{\sqrt{(\mu_p^1)^2+(\mu_q^2)^2}},\qquad (p,q)\in\mathcal{T}_{MK}, \tag{4.19}$$

where $(\widehat{|\phi^n|^2})_{pq}^s$ is the sine transform coefficient of $|\phi(\widetilde{\mathbf{x}},t_n)|^2$ (or the discrete sine transform coefficient when the values of the function $|\phi(\widetilde{\mathbf{x}},t_n)|^2$ are only available on the grid points of the bounded computational domain $\mathcal{D}$ in practical computations) at frequencies (p,q).

Combining (4.18), (4.19), and (4.10), we obtain an approximation of $\Phi(\widetilde{\mathbf{x}},t)$ in the solution (4.8) via the sine spectral method as

$$\Phi(\widetilde{\mathbf{x}},t)=\sum_{p=1}^{M-1}\sum_{q=1}^{K-1}\frac{(\widehat{|\phi^n|^2})_{pq}^s}{\sqrt{(\mu_p^1)^2+(\mu_q^2)^2}}\left[L(\mu_p^1,\mu_q^2,t)U_{p,q}(\widetilde{\mathbf{x}})+l_e^{12}(t)V_{p,q}(\widetilde{\mathbf{x}})\right], \tag{4.20}$$

where the functions $L(\xi_1,\xi_2,t)$ and $V_{p,q}(\widetilde{\mathbf{x}})$ are defined as

$$L(\xi_1,\xi_2,t)=-\left[\left(l_e^{11}(t)-l_e^{33}(t)\right)\xi_1^2+\left(l_e^{22}(t)-l_e^{33}(t)\right)\xi_2^2\right],$$
$$V_{p,q}(\widetilde{\mathbf{x}})=\partial_{\widetilde{x}\widetilde{y}}U_{p,q}(\widetilde{\mathbf{x}})=\mu_p^1\mu_q^2\cos(\mu_p^1(\widetilde{x}-a))\cos(\mu_q^2(\widetilde{y}-c)),\qquad (p,q)\in\mathcal{T}_{MK}.$$

4.2.3. Approximations in three dimensions. In the 3D case, the function $u(\widetilde{\mathbf{x}}, t_n)$ in (4.9) satisfies the Poisson equation in (1.5) which can be truncated to the computational domain $\mathcal{D}$ with homogeneous Dirichlet boundary conditions as

$$-\nabla^2 u(\widetilde{\mathbf{x}}, t_n) = |\phi(\widetilde{\mathbf{x}}, t_n)|^2, \quad \widetilde{\mathbf{x}} \in \mathcal{D}; \qquad u(\widetilde{\mathbf{x}}, t_n)|_{\partial\mathcal{D}} = 0. \tag{4.21}$$

Similarly, the above problem can be discretized by using a sine pseudospectral method in which the 0-modes are avoided. Denote the index set

$$\mathcal{T}_{MKL} = \{(p,q,r) \,|\, 1 \le p \le M-1,\ 1 \le q \le K-1,\ 1 \le r \le L-1\},$$

where $M, K, L > 0$ are integers, and define the functions

$$U_{p,q,r}(\widetilde{\mathbf{x}}) = \sin(\mu_p^1(\widetilde{x}-a))\sin(\mu_q^2(\widetilde{y}-c))\sin(\mu_r^3(\widetilde{z}-e)), \quad (p,q,r) \in \mathcal{T}_{MKL},$$

where

$$\mu_r^3 = r\pi/(f-e), \qquad 1 \le r \le L-1.$$

Again, we take the (approximate) ansatz

$$u(\widetilde{\mathbf{x}}, t_n) = \sum_{p=1}^{M-1}\sum_{q=1}^{K-1}\sum_{r=1}^{L-1} \widehat{u}_{pqr}^s(t_n)\, U_{p,q,r}(\widetilde{\mathbf{x}}), \qquad \widetilde{\mathbf{x}} = (\widetilde{x}, \widetilde{y}, \widetilde{z}) \in \mathcal{D}, \tag{4.22}$$

where $\widehat{u}_{pqr}^s(t_n)$ is the sine transform coefficient of $u(\widetilde{\mathbf{x}}, t_n)$ corresponding to frequencies (p,q,r). Substituting (4.22) into the Poisson equation (4.21) and noticing the orthogonality of the sine functions, we obtain

$$\widehat{u}_{pqr}^s(t_n) = \frac{(\widehat{|\phi^n|^2})_{pqr}^s}{(\mu_p^1)^2 + (\mu_q^2)^2 + (\mu_r^3)^2}, \qquad (p,q,r) \in \mathcal{T}_{MKL}, \tag{4.23}$$

where $(\widehat{|\phi^n|^2})_{pqr}^s$ is the discrete sine transform of $|\phi(\widetilde{\mathbf{x}}, t_n)|^2$ corresponding to frequencies (p,q,r).

Combining (4.10), (4.22), and (4.23), we obtain an approximation of $\Phi(\widetilde{\mathbf{x}}, t)$ in the solution (4.8) via the sine spectral method as

$$\begin{aligned}\Phi(\widetilde{\mathbf{x}}, t) = \sum_{p=1}^{M-1}\sum_{q=1}^{K-1}\sum_{r=1}^{L-1} \widehat{u}_{pqr}^s(t_n)\big[&L(\mu_p^1, \mu_q^2, \mu_r^3, t)U_{p,q,r}(\widetilde{\mathbf{x}}) + l_e^{12}(t)V_{p,q,r}^{(1)}(\widetilde{\mathbf{x}}) \\ &+ l_e^{13}(t)V_{p,q,r}^{(2)}(\widetilde{\mathbf{x}}) + l_e^{23}(t)V_{p,q,r}^{(3)}(\widetilde{\mathbf{x}})\big], \qquad \widetilde{\mathbf{x}} \in \mathcal{D},\end{aligned} \tag{4.24}$$

where the functions $L(\xi_1, \xi_2, \xi_3, t)$, $V_{p,q,r}^{(1)}(\widetilde{\mathbf{x}})$, $V_{p,q,r}^{(2)}(\widetilde{\mathbf{x}})$, and $V_{p,q,r}^{(3)}(\widetilde{\mathbf{x}})$ (for $(p,q,r) \in \mathcal{T}_{MKL}$) are defined as

$$\begin{aligned}
L(\xi_1, \xi_2, \xi_3, t) &= -\left[l_e^{11}(t)\xi_1^2 + l_e^{22}(t)\xi_2^2 + l_e^{33}(t)\xi_3^2\right], \\
V_{p,q,r}^{(1)}(\widetilde{\mathbf{x}}) &= \partial_{\widetilde{x}\widetilde{y}} U_{p,q,r}(\widetilde{\mathbf{x}}) = \mu_p^1\mu_q^2\cos(\mu_p^1(\widetilde{x}-a))\cos(\mu_q^2(\widetilde{y}-c))\sin(\mu_r^3(\widetilde{z}-e)), \\
V_{p,q,r}^{(2)}(\widetilde{\mathbf{x}}) &= \partial_{\widetilde{x}\widetilde{z}} U_{p,q,r}(\widetilde{\mathbf{x}}) = \mu_p^1\mu_r^3\cos(\mu_p^1(\widetilde{x}-a))\sin(\mu_q^2(\widetilde{y}-c))\cos(\mu_r^3(\widetilde{z}-e)), \\
V_{p,q,r}^{(3)}(\widetilde{\mathbf{x}}) &= \partial_{\widetilde{y}\widetilde{z}} U_{p,q,r}(\widetilde{\mathbf{x}}) = \mu_q^2\mu_r^3\sin(\mu_p^1(\widetilde{x}-a))\cos(\mu_q^2(\widetilde{y}-c))\cos(\mu_r^3(\widetilde{z}-e)).
\end{aligned}$$

Remark 4.2. After obtaining the numerical solution $\phi(\widetilde{\mathbf{x}}, t)$ on the bounded computational domain $\mathcal{D}$, we may recover the original wave function $\psi(\mathbf{x}, t)$ on a set of fixed grid points in the Cartesian coordinates $\mathbf{x}$. To this end, we may apply the standard Fourier/sine interpolation operators from the discrete numerical solution $\phi(\widetilde{\mathbf{x}}, t)$ to construct a continuous interpolating function over $\mathcal{D}$ [17, 42]. This function can then be used to compute $\psi(\mathbf{x}, t)$ over a set of fixed grid points in the Cartesian coordinates $\mathbf{x}$ for any fixed time $t \geq 0$.

Remark 4.3. If the potential $V(\mathbf{x})$ in (1.7) is replaced by a time-dependent potential, e.g., $V(\mathbf{x}, t)$, the rotating Lagrangian coordinates transformation and the numerical method are still valid provided that we replace $W(\widetilde{\mathbf{x}}, t)$ in (3.7) by $W(\widetilde{\mathbf{x}}, t) = V(A(t)\widetilde{\mathbf{x}}, t)$ for $\widetilde{\mathbf{x}} \in \mathbb{R}^d$ and $t \geq 0$.

5. Numerical results. In this section, we first test the accuracy of our numerical method and compare it with previously known methods for computing the dynamics of rotating BECs. We then study the dynamics of rotating dipolar BECs, including the center of mass, angular momentum expectation, and condensate widths. In addition, we present the dynamics of vortex lattices in rotating dipolar BEC. For simplicity, throughout this section, we consider the 2D GPE (1.7)–(1.8) with the SDM and choose the external potential $V(\mathbf{x})$ according to (1.12).

5.1. Comparisons of different methods. To test the performance of our method, we compare it with some representative methods in the literature for computing the dynamics of rotating BECs, including the Crank–Nicolson finite difference (CNFD) method [9, 29, 38], the semi-implicit finite difference (SIFD) method [9, 29], and the TSADI method [14]. Note that these methods solve the GPE in Eulerian coordinates. Here we will not compare our method with those in [11, 13], where the polar and cylindrical coordinates are used in two and three dimensions, respectively. Since different computational domains and meshes are used, it is hard to carry out a fair comparison.

We consider the 2D GPE (1.7)–(1.8) for a rotating BEC without DDI. The parameters are chosen as $d = 2$, $\Omega = 0.4$, $\gamma_x = \gamma_y = 1$, and $\eta = 0$. The initial condition of the wave function in (1.11) is taken as

$$\psi_0(\mathbf{x}) = \frac{1}{\pi^{1/4}} e^{\frac{-(x^2+2y^2)}{2}}, \qquad \mathbf{x} = (x, y)^T \in \mathbb{R}^2. \tag{5.1}$$

In our simulations, we choose a bounded computational domain $\mathcal{D} = [-8\pi, 8\pi]^2$. Let $\psi(t)$ represent the numerical solution with very fine mesh size $h_x = h_y = h = \pi/128$ and small time step $\Delta t = 0.0001$, and assume it to be a sufficiently good representation of the *exact* solution at time t. Denote $\psi^{(h_x, h_y, \Delta t)}(t)$ as the numerical solution at time t obtained with the mesh size (h_x, h_y) and time step Δt. Tables 5.1 and 5.2 show the spatial and temporal errors of different methods, where the errors are computed as $\|\psi(t) - \psi^{(h,h,\Delta t)}(t)\|_{l^2}$ at time $t = 1.5$. To calculate the spatial errors in Table 5.1, we always use a very small time step $\Delta t = 0.0001$ so that the errors from temporal discretization can be neglected compared to those from spatial discretization. Similarly, the temporal errors are obtained when a fine mesh size $h_x = h_y = \pi/128$ is used.

From Table 5.1, we see that for the same mesh size and time step, the resulting errors of TSADI and our methods are much smaller than those for the CNFD and SIFD methods. It also indicates that the CNFD and SIFD methods are second-order accurate in space while our method and TSADI are spectral-order accurate. On the

TABLE 5.1
Spatial discretization errors $\|\phi(t) - \phi^{(h_x,h_y,\Delta t)}(t)\|_{l^2}$ *at time* $t = 1.5$.

Mesh size		$\pi/4$	$\pi/8$	$\pi/16$	$\pi/32$	$\pi/64$
$\beta = 10.15$	CNFD	3.895E-1	1.475E-1	4.093E-2	9.662E-3	1.917E-3
	SIFD	3.895E-1	1.475E-1	4.093E-2	9.662E-3	1.917E-3
	TSADI	1.001E-1	1.969E-3	5.651E-8	9.391E-13	<1.0E-13
	Our method	1.031E-1	1.984E-3	5.609E-8	8.907E-13	<1.0E-13
$\beta = 32.60$	CNFD	1.2063	4.395E-1	1.722E-1	4.511E-2	8.947E-3
	SIFD	1.2064	4.394E-1	1.722E-1	4.511E-2	8.947E-3
	TSADI	3.966E-1	2.744E-2	1.875E-5	1.204E-12	<1.0E-12
	Our method	4.244E-1	2.785E-2	1.872E-5	1.146E-12	<1.0E-12
$\beta = 80.25$	CNFD	1.4181	1.3308	4.806E-1	1.888E-1	4.046E-2
	SIFD	1.4180	1.3308	4.806E-1	1.888E-1	4.046E-2
	TSADI	1.2239	1.702E-1	1.244E-3	5.208E-9	<1.0E-10
	Our method	1.3150	1.731E-1	1.244E-3	5.235E-9	<1.0E-11

TABLE 5.2
Temporal discretization errors $\|\phi(t) - \phi^{(h_x,h_y,\Delta t)}(t)\|_{l^2}$ *at time* $t = 1.5$.

Time step		1/40	1/80	1/160	1/320	1/640
$\beta = 10.15$	CNFD	1.244E-2	4.730E-3	1.195E-3	2.992E-4	7.460E-5
	SIFD	6.740E-1	3.107E-2	1.561E-2	7.915E-3	3.908E-3
	TSADI	3.510E-4	8.738E-5	2.182E-5	5.448E-6	1.358E-6
	Our method	3.433E-4	8.542E-5	2.133E-5	5.326E-6	1.327E-6
$\beta = 32.60$	CNFD	1.171E-1	3.898E-2	1.032E-2	2.601E-3	6.491E-4
	SIFD	2.589E-1	1.012E-1	3.657E-2	1.625E-2	8.196E-3
	TSADI	1.824E-3	4.510E-4	1.124E-4	2.807E-5	6.994E-6
	Our method	1.824E-3	4.481E-4	1.117E-4	2.790E-5	6.949E-6
$\beta = 80.25$	CNFD	4.716E-1	2.264E-1	7.571E-2	2.024E-2	5.089E-3
	SIFD	unstable	3.847E-1	1.790E-1	5.719E-2	1.815E-2
	TSADI	6.423E-3	1.564E-3	3.887E-4	9.697E-5	2.416E-5
	Our method	6.401E-3	1.559E-3	3.874E-4	9.663E-5	2.407E-5

other hand, Table 5.2 shows that CNFD, TSADI and our method are second-order accurate in time, while SIFD is either linear or slightly faster than linear accurate in time due to the way that we tested the temporal accuracy [5]. In fact, for the SIFD method, second-order accuracy in both space and time was observed when the mesh size and time step are decreased simultaneously [9]. In general, the spatial and temporal errors increase with the nonlinearity coefficient β when the mesh size and time step are fixed. In addition, for fixed β and time step Δt, in general, the errors from our method and TSADI are much smaller than those from CNFD and SIFD.

Compared to the SIFD and CNFD methods, our method has much higher spatial and/or temporal accuracy and is much easier to implement in practical computation. Thus for a given accuracy, the memory and computational costs of our method can be significantly reduced from those of the SIFD and CNFD methods. Similarly, compared to the TSADI method, the computational cost per time step of our method is slightly smaller. In addition, the temporal accuracy of our method can be much more easily improved to higher order, e.g., fourth order or higher, by adopting the standard higher-order time-splitting method [8, 25] since our method decomposed the GPE into two subproblems in a first-order splitting, while the TSADI has to decompose the GPE into three subproblems [11].

5.2. Dynamics of center of mass. In the following, we study the dynamics of center of mass of a rotating BEC with DDI by directly simulating the GPE (4.1)–(4.2).

To this end, we take $d = 2$, $\beta = 25\sqrt{10/\pi}$, $\eta = -\frac{15}{2}$, and dipole axis $\mathbf{n} = (1, 0, 0)^T$. The initial condition in (1.11) is taken as

$$\psi_0(\mathbf{x}) = \alpha\,\zeta(\mathbf{x} - \mathbf{x}^0) \qquad \text{with} \quad \zeta(\mathbf{x}) = (x + iy)e^{\frac{-(x^2+y^2)}{2}}, \quad \mathbf{x} \in \mathcal{D}, \tag{5.2}$$

where the constant α is chosen to satisfy the normalization condition $\|\psi_0\|^2 = 1$. We take $\mathbf{x}^0 = (1, 1)^T$. In our simulations, we use the computational domain $\mathcal{D} = [-16, 16]^2$, the mesh size $\Delta\widetilde{x} = \Delta\widetilde{y} = 1/16$, and the time step size $\Delta t = 0.0001$. We consider the following two sets of trapping frequencies: (i) $\gamma_x = \gamma_y = 1$ and (ii) $\gamma_x = 1$, $\gamma_y = 1.1$. Figure 5.1 shows the trajectory of the center of mass $\mathbf{x}_c(t)$ in the original coordinates as well as the time evolution of its coordinates for different angular velocities Ω. In addition, the numerical results are compared with analytical ones from solving the ODEs in (2.10)–(2.11).

Figure 5.1 shows that if the external trap is symmetric, i.e., $\gamma_x = \gamma_y = \gamma_r$, the center of mass always moves within a bounded region. Furthermore, if the angular velocity Ω is rational, the movement is periodic with a period depending on both the angular velocity and the trapping frequencies. In contrast, when $\gamma_x \neq \gamma_y$, the dynamics of center of mass becomes more complicated. The simulation results in Figure 5.1 are consistent with those obtained by solving the ODE system in (2.10)–(2.11) for given Ω, γ_x, and γ_y [53] and those numerical results reported in the literature by other numerical methods [11, 13, 14, 52]. In addition, our simulations show that the dynamics of center of mass are independent of the interaction coefficients β and η, which is consistent with (2.10)–(2.11).

On the other hand, we also study the dynamics of the center of mass $\widetilde{\mathbf{x}}_c(t)$ in the new coordinates. When $\gamma_x = \gamma_y$, for any Ω the center of mass has a periodic motion on the straight line segment connecting $-\widetilde{\mathbf{x}}^0 = -\mathbf{x}^0$ and $\widetilde{\mathbf{x}}^0 = \mathbf{x}^0$. This is also true for $\mathbf{x}_c(t)$ with $\Omega = 0$ (cf. Figure 5.1). However, if $\gamma_x \neq \gamma_y$, the trajectories for different Ω are very different. This observations agree with the results in (3.18)–(3.21).

5.3. Dynamics of angular momentum expectation and condensate widths. We take $d = 2$, $\Omega = 0.7$ and study the dynamics of the angular momentum expectation and condensate widths. The initial condition in (1.11) is taken as

$$\psi_0(\mathbf{x}) = \alpha\,\zeta(\mathbf{x}), \qquad \mathbf{x} \in \mathcal{D}, \tag{5.3}$$

where $\zeta(\mathbf{x})$ is defined in (5.2) and α is a constant such that $\|\psi_0\|^2 = 1$. In our simulations, we consider the following four cases:

(i) $\gamma_x = \gamma_y = 1$, $\beta = 25\sqrt{10/\pi}$, $\eta = 0$, and $\mathbf{n} = (1, 0, 0)^T$;
(ii) $\gamma_x = \gamma_y = 1$, $\beta = 15\sqrt{10/\pi}$, $\eta = -15$, and $\mathbf{n} = (1, 0, 0)^T$;
(iii) $\gamma_x = \gamma_y = 1$, $\beta = 45\sqrt{10/\pi}$, $\eta = -15$, and $\mathbf{n} = (0, 0, 1)^T$;
(iv) $\gamma_x = 1$, $\gamma_y = 1.1$, $\beta = 45\sqrt{10/\pi}$, $\eta = -15$, and $\mathbf{n} = (0, 0, 1)^T$.

In Figure 5.2, we present the dynamics of the angular momentum expectation $\langle L_z\rangle(t)$, energy $\widetilde{E}(t)$, and mass $\widetilde{N}(t)$ computed numerically from the GPE in the interval $t \in [0, 15]$. We see that if the external trap is radially symmetric in two dimensions, the angular momentum expectation is conserved when there is either no dipolar interaction (case (i)) or the dipolar axis is parallel to the z-axis (case (iii)). Otherwise, the angular momentum expectation is not conserved. The above numerical observations are consistent with the analytical results obtained from solving (2.4). In addition, we find that our method conserves the energy and mass very well during the dynamics (cf. Figure 5.2, right). Furthermore, from additional numerical results

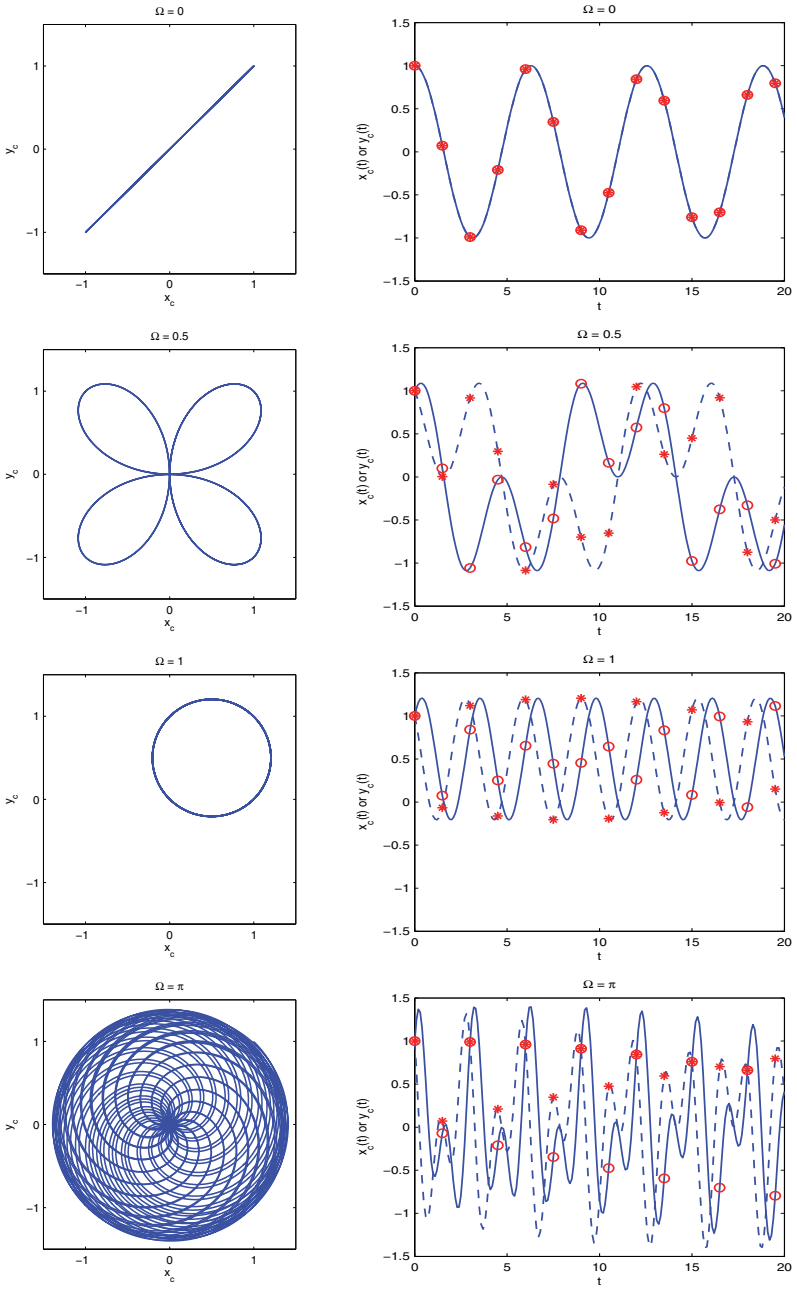

FIG. 5.1. *The dynamics of center of mass for different rotation velocity* Ω *in section* 5.2*: trajectory of the center of mass,* $\mathbf{x}_c(t) = (x_c(t), y_c(t))^T$ *for* $0 \le t \le 100$ *(left column) and coordinates of the trajectory* $\mathbf{x}_c(t)$ *(right column) (solid line:* $x_c(t)$*, dashed line:* $y_c(t)$*, where the solid and dashed lines are obtained by directly simulating the GPE and * and o represent the solutions to the ODEs in* (2.10)–(2.11)*). For case* (i) $\gamma_x = \gamma_y = 1$.

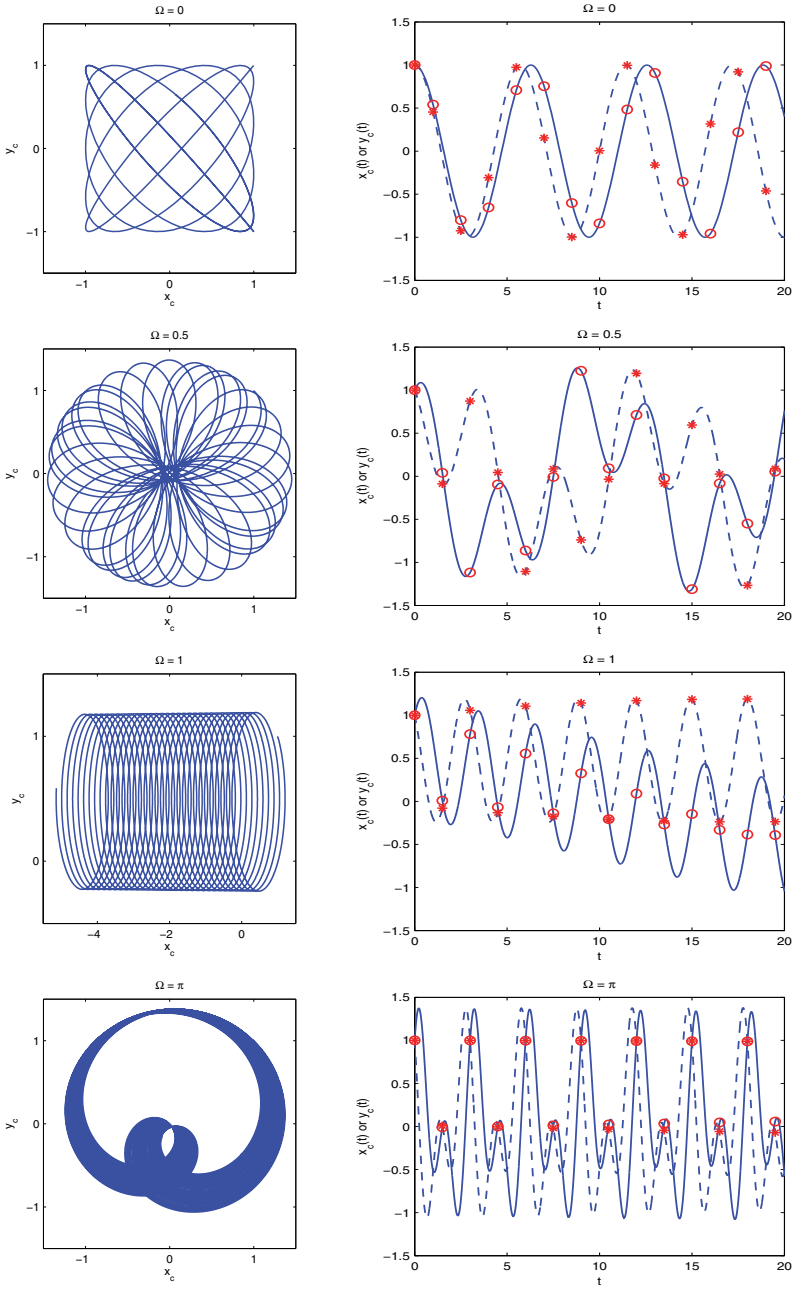

FIG. 5.1. *(cont.) For case* (ii) $\gamma_x = 1, \gamma_y = 1.1$.

not shown here for brevity, we observe that the angular momentum expectation is conserved in three dimensions for any initial data if the external trap is cylindrically symmetric and either there is no dipolar interaction or the dipolar axis is parallel to the z-axis, which can also be justified mathematically.

The dynamics of the condensate width are presented in Figure 5.3. We find that $\delta_r(t)$ is periodic as long as the trapping frequencies satisfy $\gamma_x = \gamma_y$, and the influence of

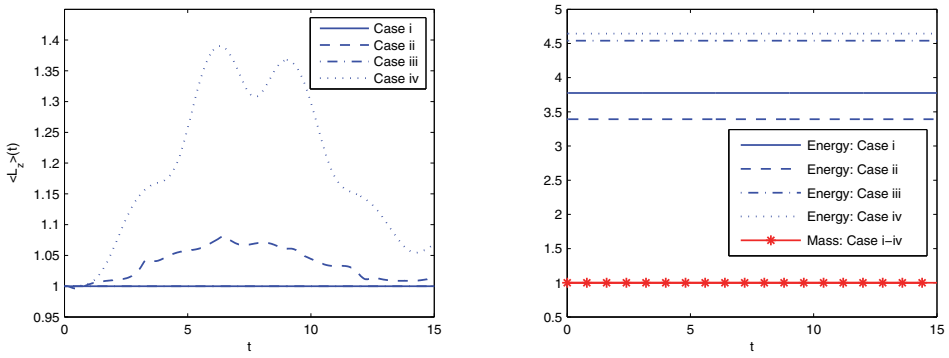

FIG. 5.2. *Time evolution of angular momentum expectation* $\langle L_z\rangle(t)$ *(left) and energy* $\widetilde{E}(t)$ *and mass* $\widetilde{N}(t)$ *(right) for Cases* (i)–(iv) *in section* 5.3. *Note that the graph of* $\langle L_z\rangle(t)$ *for Cases* (i) *and* (iii) *are identical.*

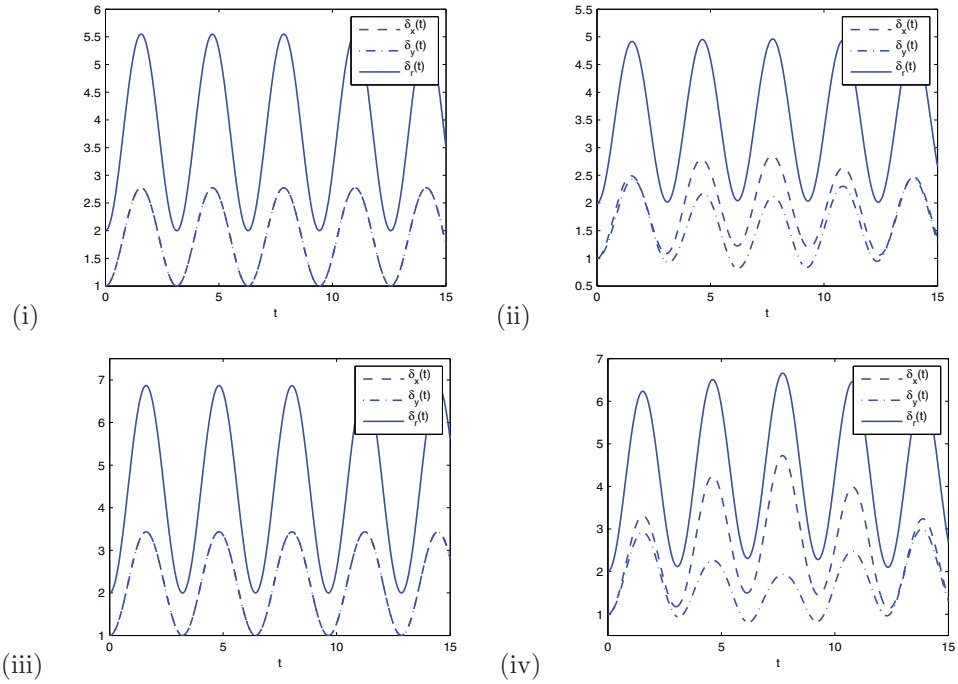

FIG. 5.3. *Time evolution of condensate widths in cases* (i)–(iv) *in section* 5.3.

the dipole axis vanishes. Furthermore, from additional numerical results not included here for brevity, we observe that $\delta_r(t)$ is periodic and $\delta_x(t) = \delta_y(t) = \frac{1}{2}\delta_r(t)$ if $\eta = 0$ for any initial data or $\mathbf{n} = (0, 0, 1)^T$ for radially symmetric or central vortex-type initial data.

5.4. Dynamics of quantized vortex lattices. In the following, we apply our numerical method to study the dynamics of quantized vortex lattices in rotating dipolar BECs. The parameters are chosen as $d = 2$, $\beta = 1000$, and $\Omega = 0.9$. The initial datum in (1.11) is chosen as a stationary vortex lattice which is computed numerically

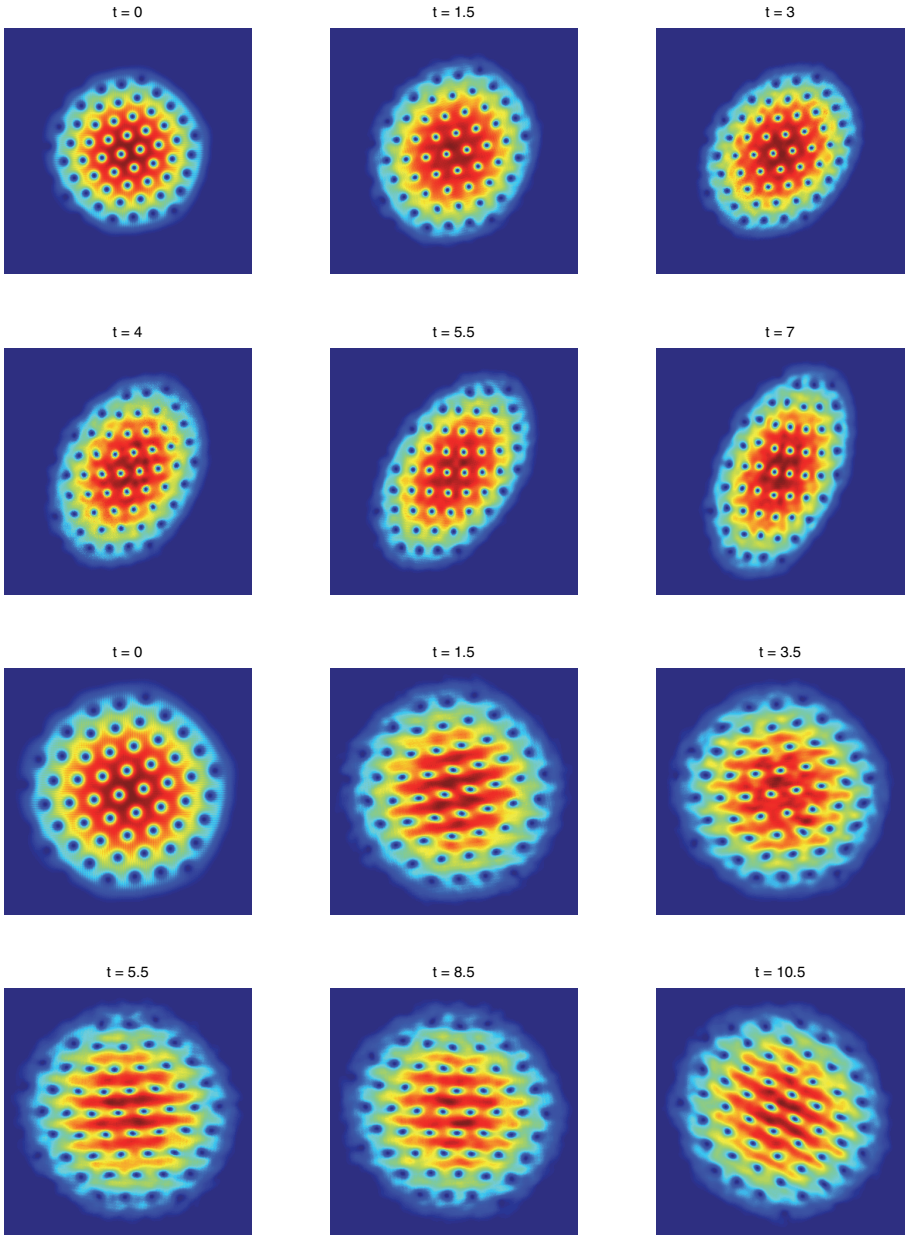

FIG. 5.4. *Contour plots of the density function* $|\psi(\mathbf{x},t)|^2$ *for the dynamics of vortex lattices in a rotating BEC in section* 5.4 *for case* (i) *(top two rows displayed on* $[-13,13]^2$*) and case* (ii) *(bottom two rows displayed on* $[-10,10]^2$*).*

via the method of [51]. Here we choose the above parameters and $\gamma_x = \gamma_y = 1$, $\eta = 0$, i.e., initially no long-range DDI. Then the dynamics of vortex lattices are studied in two cases:

(i) perturb the external potential by setting $\gamma_x = 1.05$ and $\gamma_y = 0.95$ at $t = 0$;
(ii) turn on the dipolar interaction by setting $\eta = -600$ and dipolar axis $\mathbf{n} = (1,0,0)^T$ at time $t = 0$.

In our simulations, we use $\mathcal{D} = [-16, 16]^2$, $\Delta\widetilde{x} = \Delta\widetilde{y} = 1/16$ and $\Delta t = 0.0001$. Figure 5.4 shows the contour plots of the density function $|\psi(\mathbf{x}, t)|^2$ at different times for cases (i) and (ii) where the wave function $\psi(\mathbf{x}, t)$ is obtained from $\phi(\widetilde{\mathbf{x}}, t)$ by using interpolation via sine basis (see Remark 4.2). We see that during the dynamics, the number of vortices is conserved in both cases. The lattices rotate to form different patterns because of the anisotropic external potential in case (i) and dipolar interactions in case (ii). In addition, the results in case (i) are similar to those obtained in [11], where a spectral type method in polar coordinates was used to simulate the dynamics of vortex lattices.

6. Conclusions. We proposed a simple and efficient numerical method to simulate the dynamics of rotating dipolar Bose–Einstein condensation whose properties are described by the Gross–Pitaevskii equation with both the angular momentum rotation term and the long-range dipole-dipole interaction. We eliminated the angular rotation term from the GPE by a rotating Lagrangian coordinate transformation, which makes it possible to design a simple and efficient numerical method. Based on the new mathematical formulation under the rotating Lagrangian coordinates, we designed a numerical method which combines the time-splitting techniques with Fourier/sine pseudospectral approximation to simulate the dynamics of rotating dipolar BECs. The new numerical method is explicit, unconditionally stable, spectral-order accurate in space and second-order accurate in time, and conserves the mass on the discretized level. Its temporal accuracy can be easily increased to higher order. The memory cost is $O(MK)$ in two dimensions and $O(MKL)$ in three dimensions, and the computational cost per time step is $O\left(MK\ln(MK)\right)$ in two dimensions and $O\left(MKL\ln(MKL)\right)$ in three dimensions. More specifically, the method is very easy to implement via fast Fourier transform or discrete sine transform. We reviewed some conserved quantities and dynamical laws of the GPE for rotating BECs and cast their corresponding formulations in the new rotating Lagrangian coordinates. Based on them, we numerically examined the conservation of the angular momentum expectation and studied the dynamics of condensate widths and center of mass for different angular velocities. In addition, the dynamics of vortex lattice in rotating dipolar BEC were investigated. Numerical studies showed that our method is very effective in simulating the dynamics of rotating BECs without or with DDI.

Acknowledgments. We acknowledge Professor Christof Sparber for stimulating and helpful discussions. Part of this work was done when the authors were visiting the Institute for Mathematical Sciences at the National University of Singapore in 2012.

REFERENCES

[1] M. Abad, M. Guilleumas, R. Mayol, M. Pi, and D. M. Jazek, *Vortices in Bose–Einstein condensates with dominant dipolar interactions*, Phys. Rev. A, 79 (2009), 063622.

[2] J. R. Abo-Shaeer, C. Raman, J. M. Vogels, and W. Ketterle, *Observation of vortex lattices in Bose-Einstein Condensates*, Science, 292 (2001), pp. 476–479.

[3] A. Aftalion and Q. Du, *Vortices in a rotating Bose–Einstein condensate: Critical angular velocities and energy diagrams in the Thomas–Fermi regime*, Phys. Rev. A, 64 (2001), 063603.

[4] M. H. Anderson, J. R. Ensher, M. R. Matthewa, C. E. Wieman, and E. A. Cornell, *Observation of Bose-Einstein condensation in a dilute atomic vapor*, Science, 269 (1995), pp. 198–201.

[5] X. Antoine, W. Bao, and C. Besse, *Computational methods for the dynamics of the nonlinear Schrödinger/Gross-Pitaevskii equations*, Comput. Phys. Comm., to appear.

[6] P. Antonelli, D. Marahrens, and C. Sparber, *On the Cauchy problem for nonlinear Schrödinger equations with rotation*, Discrete Contin. Dyn. Syst. A, 32 (2012), pp. 703–715.
[7] W. Bao, N. Ben Abdallah, and Y. Cai, *Gross-Pitaevskii-Poisson equations for dipolar Bose-Einstein condensate with anisotropic confinement*, SIAM J. Math. Anal., 44 (2012), pp. 1713–1741.
[8] W. Bao and Y. Cai, *Mathematical theory and numerical methods for Bose-Einstein condensation*, Kinet. Relat. Models, 6 (2013), pp. 1–135.
[9] W. Bao and Y. Cai, *Optimal error estimates of finite difference methods for the Gross-Pitaevskii equation with angular momentum rotation*, Math. Comp., 82 (2013), pp. 99–128.
[10] W. Bao, Y. Cai, and H. Wang, *Efficient numerical methods for computing ground states and dynamics of dipolar Bose-Einstein condensates*, J. Comput. Phys., 229 (2010), pp. 7874–7892.
[11] W. Bao, Q. Du, and Y. Zhang, *Dynamics of rotating Bose-Einstein condensates and its efficient and accurate numerical computation*, SIAM J. Appl. Math., 66 (2006), pp. 758–786.
[12] W. Bao, D. Jaksch, and P. A. Markowich, *Numerical solution of the Gross–Pitaevskii equation for Bose–Einstein condensation*, J. Comput. Phys., 187 (2003), pp. 318–342.
[13] W. Bao, H. Li, and J. Shen, *A generalized Laguerre-Foruier-Hermite pseudospectral method for computing the dynamics of rotating Bose–Einstein condensates*, SIAM J. Sci. Comput., 31 (2009), pp. 3685–3711.
[14] W. Bao and H. Wang, *An efficient and spectrally accurate numerical method for computing dynamics of rotating Bose–Einstein condensates*, J. Comput. Phys., 271 (2006), pp. 612–626.
[15] W. Bao and Y. Zhang, *Dynamics of the ground state and central vortex state in Bose–Einstein condensation*, Math. Models Methods Appl. Sci., 15 (2005), pp. 1863–1896.
[16] P. B. Blakie, C. Ticknor, A. S. Bradley, A. M. Martin, M. J. Davis, and Y. Kawaguchi, *Numerical method for evolving the dipolar projected Gross–Pitaevskii equation*, Phys. Rev. E, 80 (2009), 016703.
[17] J. P. Boyd, *A fast algorithm for Chebyshev, Fourier, and sinc interpolation onto an irregular grid*, J. Comput. Phys., 103 (1992), pp. 243–257.
[18] C. C. Bradley, C. A. Sackett, J. J. Tollett, and R. G. Hulet, *Evidence of Bose-Einstein condensation in an atomic gas with attractive interaction*, Phys. Rev. Lett., 75 (1995), pp. 1687–1690.
[19] V. Bretin, S. Stock, Y. Seurin, and J. Dalibard, *Fast rotation of a Bose-Einstein condensate*, Phys. Rev. Lett., 92 (2004), 050403.
[20] Y. Cai, M. Rosenkranz, Z. Lei, and W. Bao, *Mean-field regime of trapped dipolar Bose-Einstein condensates in one and two dimensions*, Phys. Rev. A, 82 (2010), 043623.
[21] M. M. Cerimele, M. L. Chiofalo, F. Pistella, S. Succi, and M. P. Tosi, *Numerical solution of the Gross–Pitaevskii equation using an explicit finite-difference scheme: An application to trapped Bose–Einstein condensates*, Phys. Rev. E, 62 (2000), pp. 1382–1389.
[22] N. R. Cooper, E. H. Rezayi, and S. H. Simon, *Vortex lattices in rotating atomic Bose gases with dipolar interactions*, Phys. Rev. Lett., 95 (2005), 200402.
[23] K. B. Davis, M. O. Mewes, M. R. Andrews, N. J. van Druten, D. S. Durfee, D. M. Kurn, and W. Ketterle, *Bose-Einstein condensation in a gas of sodium atoms*, Phys. Rev. Lett., 75 (1995), pp. 3969–3973.
[24] J. J. García-Ripoll, V. M. Pérez-García, and V. Vekslerchik, *Construction of exact solution by spatial translations in inhomogeneous nonlinear Schrödinger equations*, Phys. Rev. E, 64 (2001), 056602.
[25] R. Glowinski and P. Le Tallec, *Augmented Lagrangian and Operator Splitting Methods in Nonlinear Mechanics*, Studies in Appl. and Numer. Math. 9, SIAM, Philadelphia, 1989.
[26] K. Góral, K. Rzayewski, and T. Pfau, *Bose–Einstein condensation with magnetic dipole-dipole forces*, Phys. Rev. A, 61 (2000), 051601(R).
[27] A. Griesmaier, J. Werner, S. Hensler, J. Stuhler, and T. Pfau, *Bose–Einstein condensation of Chromium*, Phys. Rev. Lett., 94 (2005), 160401.
[28] M. Hintermüller, D. Marahrens, P. Markowich, and C. Sparber, *Optimal Bilinear Control of Gross-Pitaevskii Equations*, arXiv:1202.2306, 2012.
[29] K. Kasamatsu, M. Tsubota, and M. Ueda, *Nonlinear dynamics of vortex lattice formation in a rotating Bose–Einstein condensate*, Phys. Rev. A, 67 (2003), 033610.
[30] S. Komineas and N. R. Cooper, *Vortex lattices in Bose–Einstein condensates with dipolar interactions beyond the weak-interaction limit*, Phys. Rev. A, 75 (2007), 023623.
[31] R. K. Kumar and P. Muruganandam, *Vortex dynamics of rotating dipolar Bose–Einstein condensates*, J. Phys. B, 45 (2012), 215301.

[32] T. Lahaye, C. Menotti, L. Santos, M. Lewenstein, and T. Pfau, *The physics of dipolar bosonic quantum gases*, Rep. Progr. Phys., 72 (2009), 126401.
[33] M. Lu, N. Q. Burdick, S. H. Youn, and B. L. Lev, *Strongly dipolar Bose–Einstein condensate of Dysprosium*, Phys. Rev. Lett., 107 (2011), 190401.
[34] K. W. Madison, F. Chevy, W. Wohlleben, and J. Dalibard, *Vortex formation in a stirred Bose–Einstein condensate*, Phys. Rev. Lett., 84 (2000), pp. 806–809.
[35] K. W. Madison, F. Chevy, V. Bretin, and J. Dalibard, *Stationary states of a rotating Bose–Einstein condensates: Routes to vortex nucleation*, Phys. Rev. Lett., 86 (2001), pp. 4443–4446.
[36] F. Malet, T. Kristensen, S. M. Reimann, and G. M. Kavoulakis, *Rotational properties of dipolar Bose–Einstein condensates confined in anisotropic harmonic potential*, Phys. Rev. A, 83 (2011), 033628.
[37] M. R. Matthews, B. P. Anderson, P. C. Haljan, D. S. Hall, C. E. Wiemann, and E. A. Cornell, *Vortices in a Bose–Einstein condensate*, Phys. Rev. Lett., 83 (1999), pp. 2498–2501.
[38] P. Muruganandam and S. K. Adhikari, *Fortran programs for the time-dependent Gross–Pitaevskii equation in a fully anisotropic trap*, Comput. Phys. Commun., 180 (2009), pp. 1888–1912.
[39] C. Raman, J. R. Abo-Shaeer, J. M. Vogels, K. Xu, and W. Ketterle, *Vortex nucleation in a stirred Bose–Einstein condensate*, Phys. Rev. Lett., 87 (2001), 210402.
[40] S. Ronen, D. C. E. Bortolotti, and J. L. Bohn, *Bogoliubov modes of a dipolar condensate in a cylindrical trap*, Phys. Rev. A 74 (2006), 013623.
[41] R. Seiringer, *Ground state asymptotics of a dilute rotating gas*, J. Phys. A: Math. Gen., 36 (2003), pp. 9755–9778.
[42] J. Shen, T. Tang, and L. Wang, *Spectral Methods: Algorithms, Analysis and Applications*, Springer, New York, 2011.
[43] G. Strang, *On the construction and comparision of difference schemes*, SIAM J. Numer. Anal., 5 (1968), pp. 505–517.
[44] Q. Tang, *Numerical Studies on Quantized Vortex Dynamics in Superfluidity and Superconductivity*, Ph.D. thesis, National University of Singapore, 2013.
[45] R. P. Tiwari and A. Shukla, *A basis-set based Fortran program to solve the Gross–Pitaevskii equation for dilute Bose gases in harmonic and anharmonic traps*, Comput. Phys. Comm., 174 (2006), pp. 966–982.
[46] M. Tsubota, K. Kasamatsu, and M. Ueda, *Vortex lattice formation in a rotating Bose-Einstein condensate*, Phys. Rev. A, 65 (2002), 023603.
[47] R. M. W. van Bijnen, A. J. Dow, D. H. J. O'Dell, N. G. Parker, and A. M. Martin, *Exact solutions and stability of rotating dipolar Bose–Einstein condensates in the Thomas–Fermi limit*, Phys. Rev. A, 80 (2009), 033617.
[48] B. Xiong, J. Gong, H. Pu, W. Bao, and B. Li, *Symmetry breaking and self-trapping of a dipolar Bose-Einstein condensate in a double-well potential*, Phys. Rev. A, 79 (2009), 013626.
[49] S. Yi and H. Pu, *Vortex structures in dipolar condensates*, Phys. Rev. A, 73 (2006), 061602(R).
[50] C. Yuce and Z. Oztas, *Off-axis vortex in a rotating dipolar Bose–Einstein condensate*, J. Phys. B, 43 (2010), 135301.
[51] R. Zeng and Y. Zhang, *Efficiently computing vortex lattices in fast rotating Bose–Einstein condensates*, Comput. Phys. Comm., 180 (2009), pp. 854–860.
[52] Y. Zhang, Numerical study of vortex interactions in Bose–Einstein condensation, Commun. Comput. Phys., 8 (2010), pp. 327–350.
[53] Y. Zhang and W. Bao, *Dynamics of the center of mass in rotating Bose-Einstein condensates*, Appl. Numer. Math., 57 (2007), pp. 697–709.
[54] J. Zhang and H. Zhai, *Vortex lattices in planar Bose-Einstein condensates with dipolar interactions*, Phys. Rev. Lett., 95 (2005), 200403.